The White Dwarf Binary Pathways Survey. V. The Gaia White Dwarf Plus AFGK Binary Sample and the Identification of 23 Close Binaries

J.-J. Ren[1], R. Raddi[2], A. Rebassa-Mansergas[2,3], M. S. Hernandez[4], S. G. Parsons[5], P. Irawati[6], P. Rittipruk[6], M. R. Schreiber[7,8], B. T. Gänsicke[9,10], S. Torres[2,3], H.-J. Wang[11,12], J.-B. Zhang[11], Y. Zhao[11], Y.-T. Zhou[13,14], Z.-W. Han[15], B. Wang[15], C. Liu[1,12], X.-W. Liu[16], Y. Wang[11], J. Zheng[11], J.-F. Wang[11,12], F. Zhao[11], K.-M. Cui[11,12], J.-R. Shi[11,12], and H. Tian[1]

[1] CAS Key Laboratory of Space Astronomy and Technology, National Astronomical Observatories, Chinese Academy of Sciences, Beijing 100101, People's Republic of China; jjren@nao.cas.cn
[2] Departament de Física, Universitat Politècnica de Catalunya, c/Esteve Terrades 5, E-08860 Castelldefels, Spain
[3] Institute for Space Studies of Catalonia, c/Gran Capità 2–4, Edif. Nexus 201, E-08034 Barcelona, Spain
[4] Instituto de Física y Astronomía, Universidad de Valparaíso, Avenida Gran Bretaña 1111, Valparaíso, Chile
[5] Department of Physics and Astronomy, University of Sheffield, Sheffield S3 7RH, UK
[6] National Astronomical Research Institute of Thailand, Sirindhorn AstroPark, Donkaew, Mae Rim, Chiang Mai 50180, Thailand
[7] Departamento de Física, Universidad Técnica Federico Santa María, Av. España 1680, Valparaíso, Chile
[8] Millennium Nucleus for Planet formation, NPF, Valparaíso, Chile
[9] Department of Physics, University of Warwick, Coventry CV4 7AL, UK
[10] Centre for Exoplanets and Habitability, University of Warwick, Coventry CV4 7AL, UK
[11] CAS Key Laboratory of Optical Astronomy, National Astronomical Observatories, Chinese Academy of Sciences, Beijing 100101, People's Republic of China
[12] University of Chinese Academy of Sciences, Beijing 100049, People's Republic of China
[13] Department of Astronomy, Peking University, Beijing 100871, People's Republic of China
[14] Kavli Institute for Astronomy and Astrophysics, Peking University, Beijing 100871, People's Republic of China
[15] Key Laboratory for the Structure and Evolution of Celestial Objects, Yunnan observatories, Chinese Academy of Sciences, Kunming 650216, Yunnan Province, People's Republic of China
[16] South-Western Institute for Astronomy Research, Yunnan University, Kunming, Yunnan, 650091, People's Republic of China

Abstract

Close white dwarf binaries consisting of a white dwarf and an A-, F-, G-, or K-type main-sequence star, henceforth close WD+AFGK binaries, are ideal systems to understand the nature of type Ia supernovae progenitors and to test binary evolution models. In this work we identify 775 WD+AFGK candidates from TGAS (The Tycho-Gaia Astrometric Solution) and Gaia Data Release 2 (DR2), a well-defined sample of stars with available parallaxes, and we measure radial velocities (RVs) for 275 of them with the aim of identifying close binaries. The RVs have been measured from high-resolution spectra obtained at the Xinglong 2.16 m Telescope and the San Pedro Mártir 2.12 m Telescope and/or from available LAMOST DR6 (low-resolution) and RAVE DR5 (medium-resolution) spectra. We identify 23 WD+AFGK systems displaying more than 3σ RV variation among 151 systems for which the measured values are obtained from different nights. Our WD+AFGK binary sample contains both AFGK dwarfs and giants, with a giant fraction ∼43%. The close binary fractions we determine for the WD+AFGK dwarf and giant samples are ≃24% and ≃15%, respectively. We also determine the stellar parameters (i.e., effective temperature, surface gravity, metallicity, mass, and radius) of the AFGK companions with available high-resolution spectra. The stellar parameter distributions of the AFGK companions that are members of close and wide binary candidates do not show statistically significant differences.

Unified Astronomy Thesaurus concepts: Close binary stars (254); White dwarf stars (1799)

Supporting material: machine-readable tables

1. Introduction

A large fraction of stars are born in binary systems (Duchêne & Kraus 2013). Thus, the study of binary evolution represents an important part in our understanding of stellar evolution. The majority (≃75%) of medium/low-mass main-sequence binaries have relatively large orbital separations, evolving as if they were single stars and never interacting (de Kool 1992; Willems & Kolb 2004). The remaining ≃25% are believed to undergo dynamically unstable mass transfer episodes, when the more massive star evolves into a red giant or asymptotic giant, which generally results in a common envelope (CE) phase

(Paczynski 1976; Iben & Livio 1993; Webbink 2008). After the ejection of the CE (Passy et al. 2012; Ricker & Taam 2012), a close post-CE binary (PCEB) is formed, which contains a compact object, usually a white dwarf (WD, that is the former core of the giant star) and a main-sequence (MS) star companion.

PCEBs evolve to shorter orbital periods through angular momentum loss driven by magnetic braking and/or gravitational wave emission. Depending upon the stellar masses and orbital separations, PCEBs may undergo a second CE stage, presumably leading to double-degenerate binaries (Nelemans et al. 2001; Breedt et al. 2017; Rebassa-Mansergas et al. 2017a; Kilic et al. 2017); or enter a semi-detached state and become cataclysmic variables (CVs; Gänsicke et al. 2009; Pala et al. 2017) or super-soft X-ray sources (SSSs; Parsons et al. 2015; Kalomeni et al. 2016). Double-degenerate binaries, CVs (most

probably the recurrent novae) and SSSs are of high interest, since they are considered to be possible progenitors of Type Ia supernova (SN Ia; Langer et al. 2000), see Parthasarathy et al. (2007) and Wang & Han (2012) for a review of the various types of promising observed SN Ia progenitors.

Although it is well established that SN Ia are related to the thermonuclear ignition of a C/O core WD, there is not yet a general consensus on the pathways leading to the explosion (Han & Podsiadlowski 2004; Wang et al. 2010; Wang 2018). This may limit the use of SN Ia as cosmological probes (Riess et al. 1998; Perlmutter et al. 1999). Up to five different scenarios have been proposed leading to the explosion of SN Ia: the single- and double-degenerate scenario, the core degenerate scenario, and the double-detonation and WD +WD collision scenario (see Soker 2018, and references therein). It is likely that all these channels contribute to the observed SN Ia population, but no current population synthesis model can reproduce both the observed SN Ia rates and delay time distributions (Maoz & Mannucci 2012; Maoz et al. 2012; Wang & Han 2012).

Depending on the mass ratio and orbital period, PCEBs with more massive (A, F, G, and early-K spectral type) MS secondary stars may either evolve through a second CE and become double-degenerates (Wang & Han 2012), or some may begin mass transfer (depends on mass retention) to explode as near/sub-Chandrasekhar SN Ia (Whelan & Iben 1973; Flörs et al. 2020). Therefore, WD+AFGK PCEBs hold the potential to statistically test which progenitor channel is more efficient for producing SN Ia, i.e., observations of detached close WD +AFGK binaries offer us the potential to simultaneously sample the progenitors of many SN Ia channels.

We have initiated a large-scale observational project dedicated to (1) identify a large sample of WD+AFGK candidates and to (2) search for systems displaying significant radial velocity (RV) variations, i.e., likely close WD+AFGK PCEBs, for measuring their orbital periods. Our goals are both predicting the future of these close binary systems to test possible SN Ia progenitor channels and constraining their past evolution to test the dependence of CE efficiency with the secondary star mass. To identify WD+AFGK binaries we have previously mined the Radial Velocity Experiment (RAVE; Kordopatis et al. 2013) and LAMOST surveys. The detailed identification methodology was presented in Parsons et al. (Paper I; 2016), which mainly uses a T_{eff} (effective temperature of the MS companion) versus FUV−NUV (the GALEX far-UV minus near-UV color) selection criteria. Until now, 430 WD+AFGK binaries have been identified from RAVE data release (DR) 4 (Paper I), and 1549 from LAMOST DR4 (Paper II; Rebassa-Mansergas et al. 2017b). Follow-up spectro-scopic observations have allowed the identification of 24 close LAMOST WD+AFGK systems displaying RV variation above the 3σ level (Paper II). The first hierarchical triple system in this White Dwarf Binary Pathways Survey, and the limited and acceptable fraction of contamination of WD+AFGK sample from hierarchical triple systems containing a WD is presented in Lagos et al. (Paper III; 2020). The final goal of this project is to present a large number of WD+AFGK binaries with measured orbital periods, see Hernandez et al. (2020, Paper IV) for the first results.

In this paper, we expand our search of WD+AFGK binaries by harvesting from the Tycho-Gaia (hereafter TGAS) catalog of stars with measured parallaxes in the first Gaia data release (DR1; Michalik et al. 2015; Lindegren et al. 2016). This sample, which we later complemented with the observations from the Gaia Data Release 2 (DR2; Gaia Collaboration et al. 2018), offers a great potential to study a statistically significant number of systems and a step toward a volume complete sample that can be built with the forthcoming third Gaia data release. We then describe our high-resolution follow-up spectroscopic observations performed at the Xinglong 2.16 m and San Pedro Mártir (SPM) 2.12 m telescopes. We determine their RVs and present the identified close binaries. We also measure the stellar parameters of the AFGK companions from our spectra and perform a statistical analysis of the properties of close and wide binary candidates.

2. The WD+AFGK Sample

2.1. Preliminary Selection from the Tycho-Gaia Astrometric Solution Catalog

The first release of the Gaia mission was presented in 2016 September (Gaia Collaboration et al. 2016b), which marked the beginning of a new era in astrometry. The combination of the Tycho-2 catalog (Høg et al. 2000) with Gaia DR1 (Gaia Collaboration et al. 2016b) led to the Tycho-Gaia astrometric solution (TGAS; Michalik et al. 2015; Gaia Collaboration et al. 2016a; Lindegren et al. 2016) catalog, which provides positions, photometry in the broad visual G band, proper motions, and parallaxes with typical accuracy (uncertainties in parallaxes typically under 1 mas) of Hipparcos level or better for about two million stars up to ∼11.5 mag.

With the aim of identifying WD+AFGK binaries within TGAS, we cross-matched a subset of sources, limited to a parallax precision of $\sigma_\varpi/\varpi \leqslant 0.15$, with the latest GALEX release (FUV ⩽ 19 mag; Bianchi et al. 2017). The resulting ≈13,000 sources were complemented with optical to infrared photometry from the AAVSO Photometric All-Sky Survey (APASS DR9; Henden et al. 2015), Two-Micron All-Sky Survey (2MASS; Skrutskie et al. 2006), and the Wide-field Infrared Survey Explorer (WISE; Wright et al. 2010). This sample was later supplemented, and reanalyzed, with the addition of Gaia DR2 photometry and parallaxes (see Section 2.2).

Using a grid of synthetic spectra from the PHOENIX library (Husser et al. 2013),[17] we estimated effective temperatures (T_{eff}), stellar radii (R), and interstellar extinction (A_V), via χ^2 minimization of the observed and modeled spectral energy distributions (SEDs). Surface gravity ($\log g$) and metallicity ([Fe/H]) are also fitted, for the benefit of reaching the best fit, although the former is typically poorly determined and the latter is a priori constrained to vary around 0.0 ± 0.5 dex; hence, they are discarded as reliable estimates. For the SED fitting, we also used the TGAS parallaxes and the total-column of dust (Schlegel et al. 1998) as external constraints, and we adopted the $R_V = 3.1$ wavelength-dependent reddening law of Fitzpatrick (1999). Initially we undertook a *brute force* approach, evaluating the χ^2 at each point of a tailored grid of models, followed by a Nelder–Mead method to identify the best fit. Both methods are implemented in the PYTHON's SCIPY (Virtanen et al. 2020) and LMFIT packages. The fitting

_____

[17] For the synthetic photometry we used the Tycho bandpass and zero-points, and 2MASS zero-points determined by Maíz Apellániz (2006), APASS zero-points by Munari et al. (2014), and WISE zero-points as prescribed in the survey paper.
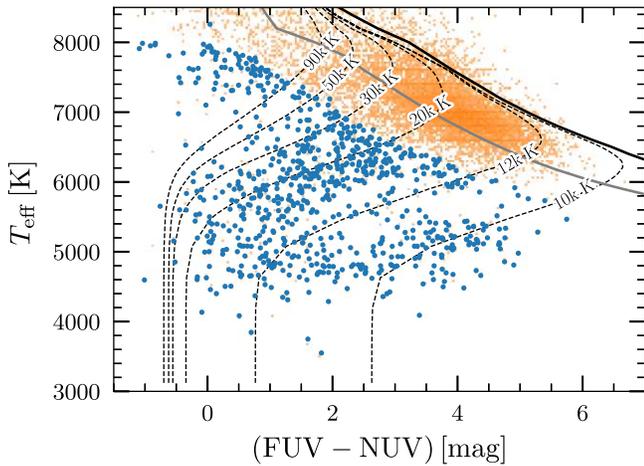
Figure 1. UV colors and photometric temperatures of ≈13,000 TGAS stars (orange cloud). Note that we only show 775 TGAS-selected candidates (blue symbols), resulting from our improved classification with Gaia DR2 and the cross-match with SIMBAD. The black and gray solid curves represent the intrinsic colors of single stars with $\log g = 4.5$, 3.5 and [Fe/H] $= 0, -1$, respectively, determined for the PHOENIX grid of synthetic models (Husser et al. 2013). The dashed black curves represent the intrinsic colors of unresolved WD+AFGK binaries for a range of WD temperatures (shown in figure) determined from $\log g = 8$ synthetic models (Koester 2010).

procedure excluded the GALEX FUV and NUV bands, where the optically brighter AFGK stars are assumed to contribute less than their WD companions.

Thus, adopting a similar, although more relaxed selection criterion as defined in Paper I, we identified as possible WD +AFGK candidates 985 stars with $T_{\rm eff} \leqslant 8000$ K and 1.5 mag bluer than the intrinsic FUV − NUV colors of PHOENIX models with $\log g = 3.5$ and [Fe/H] $= -1$. This cut enables us to remove typically metal-poor, nonbinary systems that constitute the majority of the TGAS sample (see Figure 1).

2.2. Cross-match with the Second Data Release of Gaia

Two years after the release of TGAS, the second data release of Gaia made available $G_{\rm BP}$ and $G_{\rm RP}$ photometry and improved astrometry for all our previously selected binary candidates. The new data caused a significant improvement, of which we have taken advantage for the refinement of the TGAS WD+AFGK candidate selection via the SED-fitting procedure described in the previous section. We adopted the Gaia DR2 parallax zero-point of −0.029 mas (Lindegren et al. 2018) and the revised passbands, G-band correction, and zero-points (Maíz Apellániz & Weiler 2018). We also used new 2MASS zero-points (Maíz Apellániz & Pantaleoni González 2018). Because of the high-precision of the Gaia-DR2 parallaxes, adopting $d \propto \varpi^{-1}$ is an accurate approximation of the distance estimates provided by Bailer-Jones et al. (2018). This refined sample contains 814 WD +AFGK candidates (Figure 1). In addition, we estimated the uncertainties of photometrically determined stellar parameters by using the PYTHON Markov Chain Monte Carlo sampler (EMCEE; Foreman-Mackey et al. 2019). Table A1 contains the relevant photometric and astrometric data, as well as the results of the SED-fitting analysis.

The striking improvement delivered by Gaia DR2 is visualized through the comparison between the TGAS and Gaia DR2 Hertzsprung–Russell (HR) diagrams in Figure 2, where main-sequence and giant stars can be unequivocally identified (as noted in Table A1). In addition, the Gaia DR2
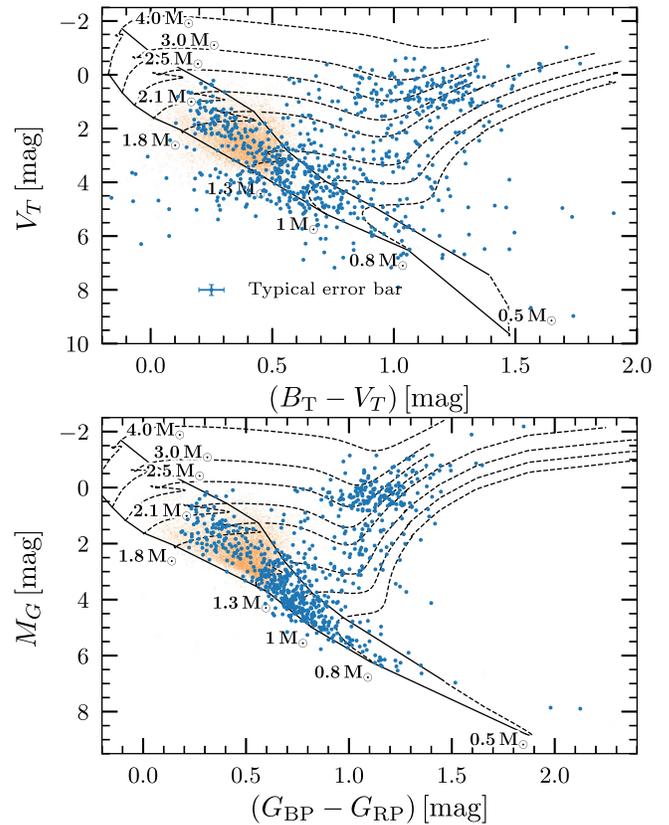

Figure 2. HR diagrams for the ≈13,000 cross-matched TGAS-GALEX stars (orange dots), which use the TGAS and Gaia DR2 data (top and bottom panels, respectively). Symbols and colors as in Figure 1. The overlaid dashed curves are the MESA/MIST evolutionary tracks, while the black solid curves represent the zero-age and the terminal-age main sequences (ZAMS and TAMS, respectively; Choi et al. 2016). In Table A1 we label as dwarfs/giants all stars below/above the TAMS track.

parallaxes can also be used to construct a GALEX HR diagram, showing that the contamination of our sample from other compact UV-bright objects, like the hot-subdwarf stars (Geier 2020), is minimal (see Figure 3).

2.3. Cross-match with SIMBAD

We cross-match the 814 selected WD+AFGK candidates with SIMBAD (Wenger et al. 2000), to obtain their SIMBAD classifications. Most of our systems are classified as "Star" or "High proper-motion Star." There are also 36 WD+AFGK candidates that are classified as "Carbon star" (1), "Classical Cepheid" (1), "CV DQ Her type" (1), "Eclipsing binaries" (19), "Eruptive variable star" (2), "Galaxy" (1), "Herbig Ae/Be star" (1), "Horizontal branch star" (1), "Hot subdwarf" (2), "Nova-like star" (1), "Planetary nebula" (1), "Pulsating variable star" (2), "T Tau-type star" (1), and "Variable star of RR Lyr type" (2). We exclude these 36 "possible contaminants" from our WD+AFGK sample, which is thus reduced to 778 systems.

Furthermore, of the 778 systems, there are three candidates (TYC 3793-959-1, TYC 265-1112-1, and TYC 2523-2620-1), which are reclassified as contaminants (MS binaries or triple systems harboring two MS stars and a WD) by us later after investigating our follow-up high-resolution spectra (displaying double-lines), which will be published in a forthcoming paper. Thus, there are in total 39 "possible contaminants" in our sample. After excluding them, we finally obtain 775 WD
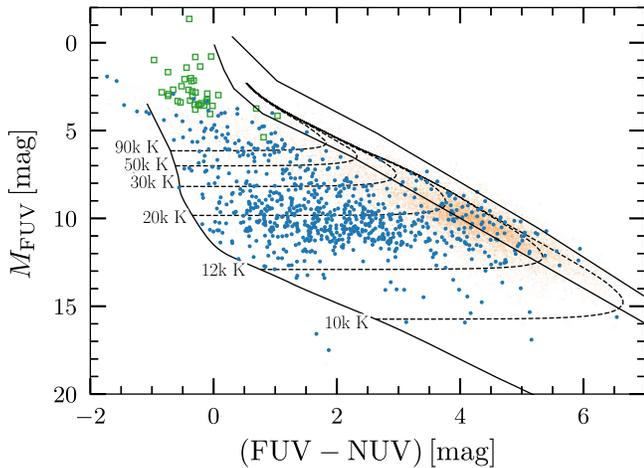
Figure 3. GALEX HR diagram. Symbols and colors as in Figure 2 for the TGAS-GALEX cross-matched stars and our 775 WD+AFGK candidates. Hot subdwarf with AFGKM companions (Geier 2020) are plotted as green squares. The intrinsic magnitudes and colors of $\log g = 8$ WDs are shown on the left as a solid black curve, while the composite colors and absolute magnitudes of WD+AFGK binaries are plotted as dashed curves. The solar-metallicity ZAMS and TAMS are plotted as in Figure 2.

+AFGK candidates. The SIMBAD classification information of the 775 WD+AFGK candidates and 39 excluded "possible contaminants" are listed in Table A1.

2.4. Cross-match with RAVE DR5 and LAMOST DR6

RAVE is a multifiber spectroscopic astronomical survey of stars in the Milky Way. It is operated through the 1.2 m UK Schmidt Telescope of the Australian Astronomical Observatory (AAO). As a southern hemisphere survey, RAVE covers 20,000 square degrees of the sky. The primary aim of RAVE is to derive the RVs, stellar parameters, and elemental abundances of stars to study the structure, formation and evolution of our Milky Way (Kunder et al. 2017). RAVE targets bright stars in the magnitude range $8 < I < 12$ mag. The RAVE spectra cover the spectral region 8410–8794 Å, which contains the infrared calcium triplet, with a resolving power of $R \sim 7500$. This allows obtaining RVs with a median precision better than 1.5 km s^{-1} and good precision stellar atmospheric parameters and chemical abundances (Kunder et al. 2017). RAVE largely overlaps with TGAS, i.e., 249,603 spectra of 215,590 unique TGAS stars have been observed by RAVE. By comparing our WD+AFGK list with the newest release of RAVE (i.e., DR5; Kunder et al. 2017), we found 104 systems in common (corresponding to 125 RAVE spectra, marked in the "Spec" column in Table A1).

LAMOST is a quasi-meridian reflecting Schmidt telescope of ~ 4 m effective aperture and a field of view of 5 deg in diameter (Cui et al. 2012; Liu et al. 2020), located in Xinglong station of National Astronomical Observatories, Chinese Academy of Sciences. Being a dedicated large-scale survey telescope, LAMOST uses 4000 fibers to obtain spectra of celestial objects as well as sky background and calibration sources in one single exposure. LAMOST spectra cover the entire optical wavelength range ($\simeq 3700$–9000 Å) at a resolving power $R \sim 1800$ (Luo et al. 2015). LAMOST DR6 low-resolution spectroscopic survey has made use of 4577 plates, of which 75% are VB/B plates (very bright plates: $r \leqslant 14$ mag, bright plates: 14 mag $\leqslant r \leqslant 16.8$ mag), 41% are VB plates, similar to those summarized in Ren et al. (2018). Thus, a large fraction of stars observed by LAMOST are bright. By cross-

Table 1
Summary of the WD+AFGK Candidates Identified in This Work

Name	Number
Total number of sources with UV colors and photometric T_{eff}	$\approx$13,000
The initial selected WD+AFGK candidates in TGAS	985
The Gaia DR2 refined sample of WD+AFGK candidates	814
The final sample after removing contaminants	775
with available RAVE DR5 spectra	104
with available LAMOST DR6 spectra	82

matching our WD+AFGK binary list with LAMOST DR6, we found 82 targets in common (corresponding to 138 LAMOST spectra, see the "Spec" column in Table A1).

Table 1 presents a summary of our WD+AFGK sample. As mentioned in Section 2.3, after excluding the 37 "possible contaminants," we obtain a sample containing 775 WD+AFGK candidates. Of them, 37 and 20 candidates have been published in our previous RAVE DR4 (Paper I) and LAMOST DR4 WD+AFGK sample (Paper II), respectively. The last column of Table A1 marks those already published before. Therefore, 718 are new WD+AFGK candidates, of which 67 have the new available RAVE DR5 spectra and 62 have the LAMOST DR6 spectra (see Table A2 for the detailed information), all of which will be used in our following RV measurements.

3. Observations

As demonstrated in Paper II, high-resolution spectra are needed to efficiently identify low inclination ($\lesssim$5 deg) and/or long orbital period systems ($\gtrsim$100 days), which is especially important for identifying systems that will evolve through a second CE phase and thus become SN Ia double-degenerate progenitor candidates. Our observations were hence carried out by using the Xinglong 2.16 m telescope (hereafter, XL216; Fan et al. 2016) and the San Pedro Mártir 2.12 m telescope, both equipped with Echelle spectrographs.

We observed 93 WD+AFGK candidates during 23 nights from the XL216. The observing log is summarized in Table 2. The instrument terminal we used was the High Resolution fiber-fed Spectrograph (HRS), thus providing Echelle spectra of a 49,800 resolving power for a fixed slit width of 0.19 mm, and covering the $\sim$3650–10000 Å wavelength range (Fan et al. 2016). The Thorium–Argon (hereafter, Th–Ar) arc spectra were taken at the beginning and end of each night. The HRS works in a very stable environment, where the temperature is quite stable. The stability of the HRS instrument for the RV measurement is rms $= \pm 6$ m s^{-1} (Fan et al. 2016). 214 spectra were obtained for 93 WD+AFGK candidates, of which 92 were observed at least twice and on different nights. Only one system (TYC 4698-895-1) was observed just once. The spectra were reduced by using the IRAF package (Tody 1986, 1993) following the standard procedures: bias subtraction, flat-field correction, scattered-light subtraction, spectra extraction, wavelength calibration (based on Th–Ar arc spectra), and continuum normalization (by using the IRAF task "continuum" order by order).

Eight nights of observations were carried out using the Echelle spectrograph attached to the 2.12 m telescope at the San Pedro Mártir Observatory in Baja California, México. The corresponding resolving power is $R \sim 20,000$ for a slit width of $2\rlap{.}{''}8$, covering the 3650–7300 Å wavelength range. Arc spectra were taken before and after each object. 50 high-resolution spectra were obtained for 22 WD+AFGK candidates, of which

Table 2
The Observation Summary of High-resolution Spectroscopy

Date	$N_{\rm Spec}$	Telescope	Weather	Seeing (arcsec)	Exposure Time (s)	S/N
20170706	3	SPM+Echelle	cirrus	1.6	$\simeq$1200	5–10
20170709	3	SPM+Echelle	cirrus	1.8	$\simeq$1200	5–10
20170710	1	SPM+Echelle	cirrus	1.6	$\simeq$1200	13
20170711	1	SPM+Echelle	cirrus	1.6	$\simeq$1200	13
20171202	18	XL216+HRS	clear	2.3	100–2400	25–100
20171203	15	XL216+HRS	clear	2.7	400–3300	25–80
20171204	18	XL216+HRS	clear	2.5	200–2400	25–80
20180104	9	XL216+HRS	cloudy	2.5	400–3600	25–110
20180110	10	SPM+Echelle	cloudy/windy	2.1	$\simeq$1200	10–20
20180110	4	XL216+HRS	clear	3.5	360–3600	25–40
20180111	3	SPM+Echelle	cloudy/windy	1.8	$\simeq$1200	10–22
20180111	19	XL216+HRS	clear	2.5	100–1200	10–50
20180112	10	SPM+Echelle	cloudy/windy	1.8	$\simeq$1200	12–19
20180113	9	SPM+Echelle	cirrus/windy	1.8	$\simeq$1200	9–16
20180114	5	SPM+Echelle	clear	1.3	$\simeq$1200	11–21
20180116	5	SPM+Echelle	cirrus	1.8	$\simeq$1200	9–18
20180220	19	XL216+HRS	cloudy	2.0	40–2400	25–90
20180221	15	XL216+HRS	clear	2.0	500–2400	30–70
20180222	13	XL216+HRS	cloudy	2.0	100–2400	25–65
20180225	3	XL216+HRS	cloudy	2.0	900–2400	25–80
20180226	15	XL216+HRS	clear	2.0	400–1400	25–45
20180305	3	XL216+HRS	clear	4.0	3600	27–37
20180502	9	XL216+HRS	clear	2.3	200–1800	22–50
20180503	13	XL216+HRS	clear	2.0	180–1400	14–50
20180504	4	XL216+HRS	cloudy	2.0	1200–3000	20–30
20180505	5	XL216+HRS	cloudy	2.2	300–3300	20–40
20180506	8	XL216+HRS	cloudy	2.0	900–3000	20–37
20180527	4	XL216+HRS	cloudy	2.1	1800–2400	15–39
20180601	6	XL216+HRS	clear	2.1	400–2400	29–40
20180602	3	XL216+HRS	cloudy	2.2	1000–3600	22–49
20180607	6	XL216+HRS	clear	2.5	30–1500	28–65
20180626	2	XL216+HRS	clear	2.5	1800–3600	35–40
20180627	3	XL216+HRS	clear	2.1	1200–1800	40–46

Note. In this table we list the observational date, the number of spectra obtained per night, the instruments (telescopes and spectrographs) we used, the corresponding weather, seeing, exposure time range, and S/N range (S/N is estimated at ∼8500 Å for XL216+HRS spectrum, and ∼6000 Å for SPM+Echelle spectrum) during the observations.

18 have at least two spectra obtained on different nights. The data reduction procedures of SPM spectra are the same as the XL216 spectra.

To summarize, we obtained 264 high-resolution spectra for 104 WD+AFGK candidates, each of them having at least two spectra obtained on different nights.

4. Radial Velocity Measurements

4.1. High-resolution Spectra

We measured the RVs from the 214 spectra obtained from the XL216 telescope by fitting the normalized Ca II absorption triplet (at 8498.03, 8542.09, and 8662.14 Å) with a combination of a second-order polynomial and a triple-Gaussian profile of fixed separations, as described in Paper II. Only when the Ca II absorption triplet was too noisy to get a reliable RV, then the normalized Na I doublet at ∼5890 Å (i.e., 5889.951 and 5895.924 Å) was used. In this case we used a second-order polynomial and a double-Gaussian profile of fixed separation. The RV uncertainty is obtained by summing the fitted error and a systematic error of 0.5 km s^{-1} in quadrature, which is an appropriate value for spectra of signal-to-noise ratio (S/N) ∼ 25–30, based on our experience with this instrument.

An example of double-Gaussian fit to the Na I doublet profile and triple-Gaussian fit to the Ca II triplet profile can be seen in Figure 4. Figure 5 shows a comparison between the RVs determined from Ca II triplet and the Na I doublet from the same spectra, which are in good agreement despite the fact that the Na I feature is usually affected by interstellar absorption.

Given that the SPM spectra only cover the 3650–7300 Å wavelength range, the RVs are determined by fitting the Na I doublet. The RV uncertainty is obtained by summing up the error obtained from the fit and a systematic error of 1 km s^{-1} ($R \sim 20{,}000$) in quadrature.

4.2. RVs from RAVE/LAMOST Spectra

The RVs of the 104 WD+AFGK candidates with 125 RAVE spectra are taken from the DR5 catalog (Kunder et al. 2017), which are determined by an automatic pipeline using a standard cross-correlation procedure. For the RAVE RV uncertainties, we incorporate a systematic error of 3 km s^{-1} due to the medium resolution ($R \sim 7500$) of RAVE spectra. For the 138 LAMOST spectra of 82 candidates as mentioned in Section 2. We measured the RVs for 128 good quality spectra of 80 WD+AFGK candidates by fitting the Ca II absorption
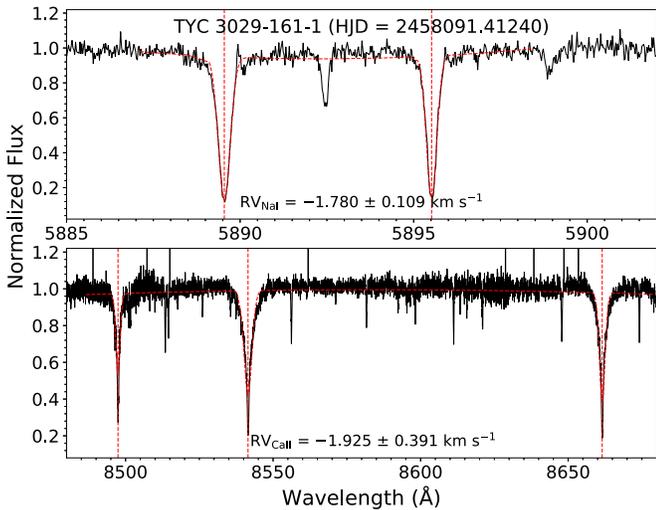
Figure 4. Line fitting examples for the Na I D doublet (top panel) and Ca II triplet (bottom panel) profile of a high-resolution spectrum from XL216 telescope. The vertical red dashed line shows the fitted line center. The fitted RVs and fitting errors are shown in the figure too.
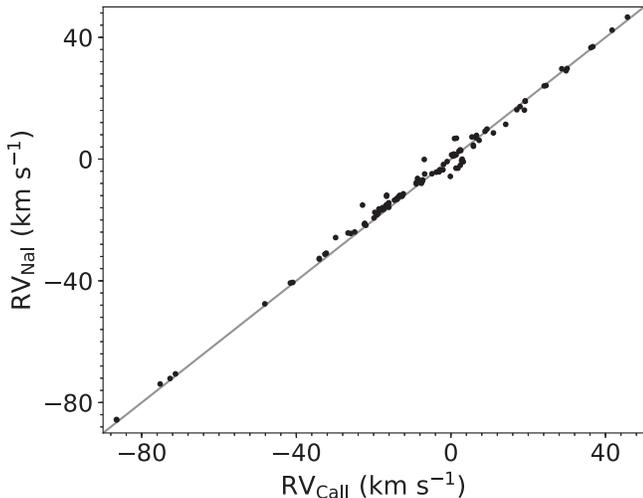

Figure 5. Comparison of RVs determined by fitting Ca II triplet and Na I doublet for the 112 spectra observed with the XL216.

triplet; the quality of the other 10 spectra is too bad to measure RVs. For the LAMOST RV uncertainties, the systematic error we incorporate is 10 km s^{-1} (Luo et al. 2015).

4.3. The Final RV Table

By including all the RVs determined from the previous subsections, we have obtained 517 RV values for 275 WD+AFGK candidates. All the RVs are listed in Table 3, which presents the corresponding Heliocentric Julian Dates (HJD), the RVs and corresponding errors (fitting and total errors), and the telescopes used for obtaining the spectra. In summary, for the 275 WD+AFGK candidates with available RVs, 154 targets have at least two RVs, 151 have at least two RVs separated by one night (i.e., only three targets have two RVs on the same night), and 121 have only one RV value (which is either from LAMOST or RAVE). Most importantly, for the 264 RVs (104 targets) obtained from XL216/SPM high-resolution spectral follow-up, all 104 targets have at least two RVs separated by

one night. Table 4 presents the statistics of all the 517 RVs from different telescopes.

4.4. Confirmed Radial Velocity Variables

We use the RVs from Table 3 to identify close binaries. That is, a given system will be considered as a close binary if we detect significant (i.e., $>3\sigma$) RV variation (Rebassa-Mansergas et al. 2007; Ren et al. 2013). Conversely, if no RV variation is detected from spectra observed in at least two different nights, the system is considered as a likely wide binary candidate.

We identify 23 RV variable AFGK stars (displaying more than 3σ RV variation), which are suggested to be members of close binary systems; the remaining 128 targets are suggested to be likely wide binary members. Table 5 gives the detailed number of close/wide WD+AFGK candidates identified from different telescopes.

Table 6 lists the 23 close binaries and the corresponding telescopes used to detect them, as well as the maximum RV shift measured and the corresponding time span between the observations. Figure 6 plots the maximum RV shift versus time span for the 23 close binaries. We can see that the maximum RV shifts vary from ~4 to 160 km s^{-1}. The close binaries with RV shifts as small as 4 km s^{-1} were detected from our highest resolution ($R \sim 49,800$) spectra (i.e., XL216 data, red open circles in Figure 6), which agree with the statement of Paper II claiming that high-resolution spectra are needed to identify close binaries with small RV variations (i.e., these systems have long orbital periods and/or low orbital inclinations; see Figure 5 in Paper II). Furthermore, most of our close binaries have the time baseline shorter than ~100 days, as our follow-up observations were performed within half a year. Only four systems detected from survey data (i.e., LAMOST/RAVE) have considerably longer time baselines.

5. Stellar Parameters

5.1. Dwarf/Giant Classification

When selecting TGAS WD+AFGK binaries, we only used the $T_{\rm eff}$ versus FUV−NUV diagram, without applying a log g cut. Thus, our WD+AFGK binary sample contains both AFGK dwarfs and giants.

The dwarf/giant classification is based on the Gaia DR2 HR diagram. As inferred from the bottom panel of Figure 2, the stars below/above the TAMS are classified as dwarfs/giants, respectively. The dwarf/giant classification is flagged in Table A1. Of the 775 WD+AFGK binaries that form our sample, 443/332 are classified as dwarfs/giants, i.e., a giant fraction of ~43%. Among the 23 close WD+AFGK candidates we identified (as shown in Table 6), 10 are giants, which corresponds to a giant fraction ~43% for close systems. We will discuss the close binary fractions of WD+AFGK binaries containing dwarf and giant stars in Section 6.

5.2. Stellar Parameters from RAVE/LAMOST Spectra

For those WD+AFGK binaries with available RAVE DR5 medium-resolution spectra, the stellar atmospheric parameters and chemical abundances of their companions were adopted from Kunder et al. (2017), who used the same stellar parameter pipeline as in DR4, but calibrated using recent K2 Campaign 1 seismic gravities and Gaia benchmark stars, as well as results obtained from high-resolution studies. The typical uncertainties

Table 3
The RV Table of the 275 WD+AFGK Candidates

Name	HJD (days)	RV (km s^{-1})	Err$_{fit}$ (km s^{-1})	Err$_{tot}$ (km s^{-1})	Telescope
TYC 1006-4-1	2458170.36445	−18.854	0.419	0.652	XL216
TYC 1006-4-1	2458172.30624	−19.139	0.469	0.685	XL216
TYC 1010-403-1	2457860.34272	−16.685	5.696	11.509	LAMOST
TYC 1010-403-1	2457917.19322	−26.570	4.586	11.001	LAMOST
TYC 1020-875-1	2457528.30082	−18.835	2.986	10.436	LAMOST
TYC 110-755-1	2458170.07184	−37.246	0.255	0.561	XL216
TYC 110-755-1	2458176.04568	−42.918	0.589	0.772	XL216
TYC 1131-1838-1	2458272.28582	−7.703	0.334	0.601	XL216
TYC 1131-1838-1	2458277.31122	−7.257	0.241	0.555	XL216
TYC 1191-179-1	2457941.89752	10.143	0.477	1.108	SPM
…	…	…	…	…	…

Note. This table also lists the HJD, and the telescopes (i.e., XL216, SPM, LAMOST, RAVE) used for obtaining the spectra.

(This table is available in its entirety in machine-readable form.)

Table 4
The Number Statistics of Available RVs of WD+AFGK Candidates from Different Telescopes

Telescope	N_{RVs}	N_{target}	$N_{\geqslant 2\,RVs}^{targets}$
XL216	214	93	92
SPM	50	22	18
XL216+SPM	264	104[a]	104
RAVE	125	104[b]	20
LAMOST	128	80[c]	29
Total	517	275	151

Notes. This table shows the number statistics of available RVs for different RV origins for 275 WD+AFGK candidates, which includes the telescopes, number of RVs, the corresponding target number, and the number of targets with at least two RVs separated by one night.
[a] Note that 11 targets were both observed by XL216 and SPM.
[b] One of them was also observed by XL216, and one by SPM.
[c] Nine of them were also observed by XL216, two by SPM.

Table 5
The Number of Close/Wide System Candidates Detected from Different Telescopes in This Work

Type	XL216/SPM	RAVE	LAMOST	Total
Close	19	3	1	23
Wide	85	17	26	128
Close+Wide	104	20	27	151

Note. This table shows the statistics of close/wide system candidates detected from different telescopes.

Table 6
The Information of the 23 Close Binaries Identified in This Work

Name	Max RV Shift (km s^{-1})	Time Span (days)	Detect from
TYC 110-755-1	5.672	5.97384	XL216
TYC 1223-498-1	20.254	10.63028	XL216
TYC 1380-957-1	66.925	5.09723	XL216
TYC 1394-1008-1	13.350	40.14194	XL216
TYC 1428-81-1	30.225	5.12495	SPM
TYC 1655-707-1	34.656	18.97566	XL216
TYC 2292-1379-1	6.178	40.73237	XL216+SPM
TYC 278-239-1	8.445	2.09796	SPM
TYC 2850-1366-1	20.429	1.90052	XL216
TYC 3104-932-1	13.294	25.02232	XL216
TYC 3814-455-1	66.084	681.05243	LAMOST
TYC 3883-1104-1	3.964	125.86194	XL216
TYC 418-2364-1	5.987	70.98452	XL216
TYC 4564-627-1	40.447	61.80570	XL216
TYC 4700-815-1	55.650	77.90281	XL216
TYC 4717-255-1	5.763	42.55069	XL216+SPM
TYC 5523-324-1	7.167	0.87083	SPM
TYC 5856-1958-1	21.590	1429.05347	RAVE
TYC 7443-1018-1	54.294	765.94586	RAVE
TYC 841-433-1	34.559	70.82929	XL216
TYC 856-918-1	7.422	1.97168	SPM
TYC 8873-148-1	163.580	229.34639	RAVE
TYC 969-1420-1	55.438	167.17345	SPM

Note. This table lists the maximum RV shift and the corresponding time span for the 23 close binaries. The telescopes used to detect the close binaries are also listed.

in T_{eff}, $\log g$, and [M/H] are approximately 250 K, 0.4 dex, and 0.2 dex, respectively, but vary with stellar population and S/N. The stellar parameters of the 104 WD+AFGK binaries (125 RAVE spectra) are listed in Table A2 in the Appendix.

The stellar parameters of the TGAS-LAMOST WD+AFGK candidates were determined from the LAMOST Stellar Parameter pipeline (LASP; Luo et al. 2015). LASP determines the stellar parameters by template matching with the ELODIE empirical library (Prugniel & Soubiran 2001). The stellar parameters of the AFGK companions of 82 WD+AFGK binaries are listed in Table A2 of the Appendix too.

In brief, of the 186 WD+AFGK binaries with available RAVE/LAMOST spectra shown in Table A2, 154 have available RAVE/LAMOST stellar parameters and S/N > 30. Their $\log g$ versus T_{eff} diagram is shown in Figure 7. The black/red dots in Figure 3 flag the dwarfs/giants classified in Section 5.1. The $\log g$ versus T_{eff} diagram based on the RAVE/LAMOST stellar parameters roughly agrees with our dwarf/giant classification based on the Gaia DR2 HR diagram. The discrepancies should be due to the larger uncertainties of the stellar parameters measured from LAMOST and RAVE spectra. Figure 8 shows the comparison of spectroscopic T_{eff} (black/red dots for RAVE/LAMOST respectively) with
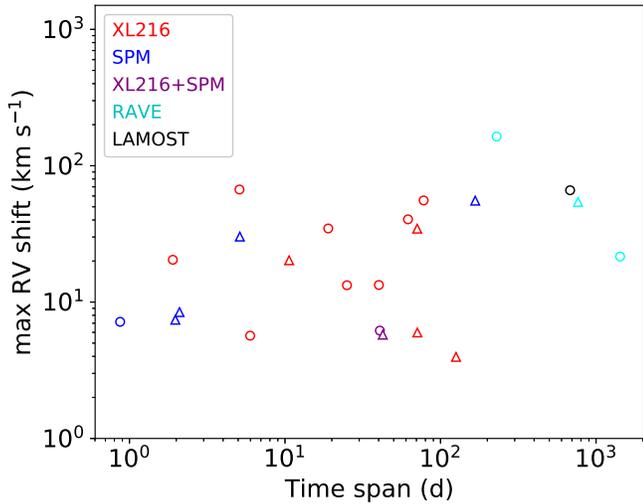
Figure 6. Maximum RV shift vs. time span for the 23 close binaries identified in this work. The circles show the dwarfs (13), while the triangles show the giants (10). Different colors show the close systems detected from different telescopes.
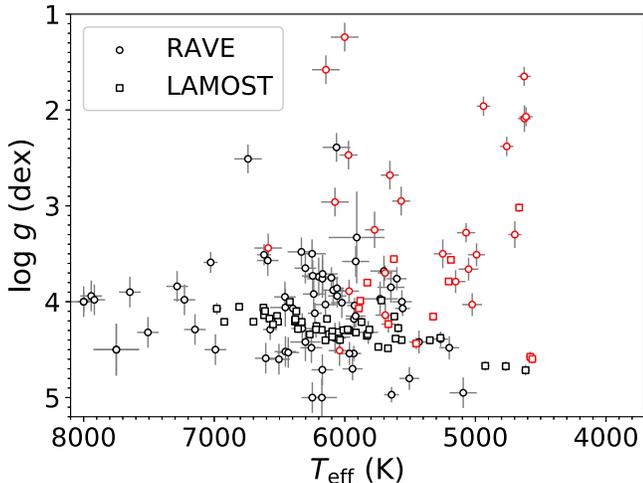

Figure 7. The $\log g$ vs. $T_{\rm eff}$ diagram for TGAS-RAVE/LAMOST WD+AFGK candidates with available RAVE/LAMOST stellar parameters (for S/N > 30). The circle/square marks the stellar parameters from RAVE/LAMOST, respectively. The black/red colors correspond to the dwarf/giant classification of Section 5.1.

photometric ones presented in Table A1. We can see large deviations between them, ~290 K, especially for high $T_{\rm eff}$ ones (hotter than ~6500 K), which further imply the relatively large uncertainties of stellar parameters from RAVE/LAMOST spectra.

5.3. High-resolution Spectroscopic Analysis

At first, we measure the stellar parameters ($T_{\rm eff}$, $\log g$, and [Fe/H]) from the high-resolution spectra of 104 WD+AFGK binaries. These were obtained by using the v2019.03.02 version of the freely distributed code iSpec (Blanco-Cuaresma et al. 2014; Blanco-Cuaresma 2019). Specifically, we used the spectral synthesis method, utilizing the radiative transfer code SPEC-TRUM (Gray & Corbally 1994), the MARCS grid of model atmospheres (Gustafsson et al. 2008), solar abundances from Grevesse et al. (2007), and the version 5 of the GES atomic line list (Heiter et al. 2015) between 420 and 920 nm. Furthermore,
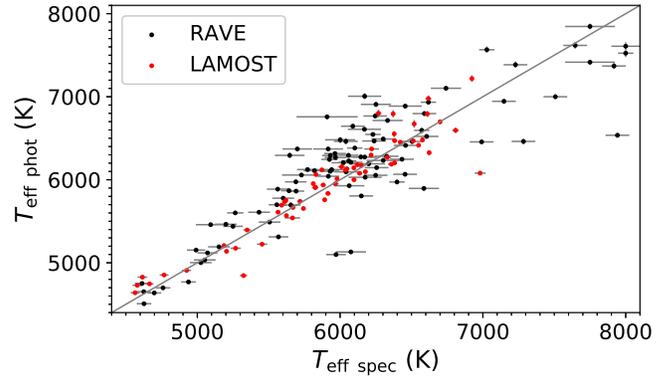

Figure 8. Comparison of spectroscopic $T_{\rm eff}$ determined from RAVE/LAMOST spectra and the photometric $T_{\rm eff}$ from Table A1. The black/red colors identify the RAVE/LAMOST samples, respectively.

before the analysis, we coadded all the duplicated spectra (after applying the RV shift correction) to increase the S/N.

When performing the fitting, the initial set of atmospheric parameters we used were the photometric $T_{\rm eff}$, $\log g$ based on SED fitting and the initial [Fe/H] was set to 0.0 dex. Because of the relatively low S/N achieved during our observations (20–30),[18] we managed to derive the stellar parameters for 55 (which have relatively good spectral quality) of the 104 stars, which are shown in Table A3.

Then the stellar masses and radii are derived by using the PARAM 1.3,[19] which is a Bayesian PARSEC-isochrones (Bressan et al. 2012) fitting code for the estimation of stellar parameters (da Silva et al. 2006). The spectroscopic $T_{\rm eff}$, $\log g$ together with the APASS V mag and Gaia DR2 parallax, are used as the input parameters to estimate the basic stellar parameters. The derived masses and radii are also listed in Table A3.

5.4. WD Contribution to the Composite SED

Following the results of the spectral analysis, we attempted to characterize the WD contribution to the composite SEDs by redoing the SED-fitting procedure (i.e., obtaining a binary SED-fit solution) and MCMC error analysis outlined in Sections 2.1–2.2; this time, we included the Koester (2010) grid of synthetic WD spectra with $\log g = 8$ (which is representative of the whole WD population) to model the contribution of the UV-bright companions. As external priors, we imposed the high-resolution spectroscopic $\log g$ and [Fe/H], Gaia DR2 parallaxes, and the single-star photometric $T_{\rm eff}$, R, and A_V. The composite SED fitting, determines the WD $T_{\rm eff}$ adapting the other parameters. Due to the large deviations of RAVE/LAMOST stellar parameters (as mentioned in Section 5.2), here the binary SED-fitting is only carried out and tested for binary systems with available high-resolution spectra.

The bottom panels of Figure 9 show an example of the binary SED fitting solution for one of our close WD+AFGK candidate (i.e., TYC 3883-1104-1). For comparison, the top panels show the corresponding single SED fitting solution. We can see that the WD $T_{\rm eff}$ can be estimated after applying the binary SED fitting solution. Figure 10 shows the correlations between fitted parameters.

---

[18] Note that these values are good enough for measuring reliable RVs.
[19] http://stev.oapd.inaf.it/cgi-bin/param_1.3

Figure 10. Corner plots of binary SED fitting solution for TYC 3883-1101-1, showing the correlations between fitted parameters. Superindex parameters "1" and "2" correspond to the AFGK and WD stars, respectively. The solid blue curves represent the 1σ contours.
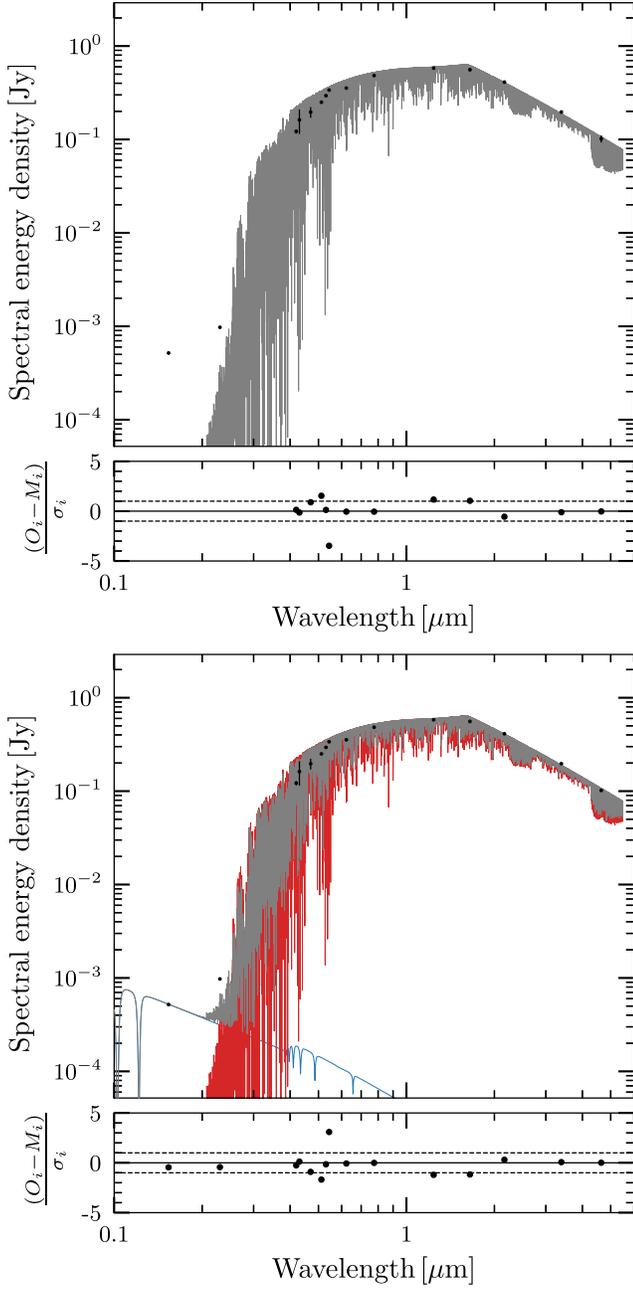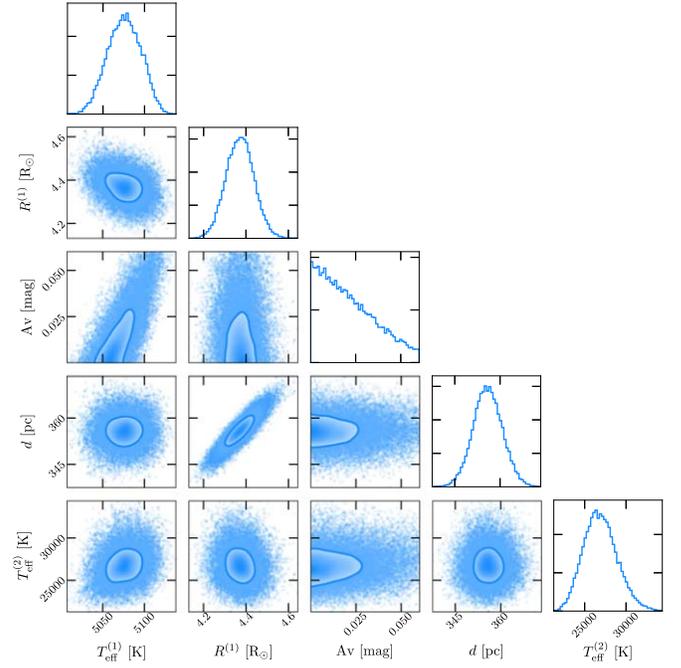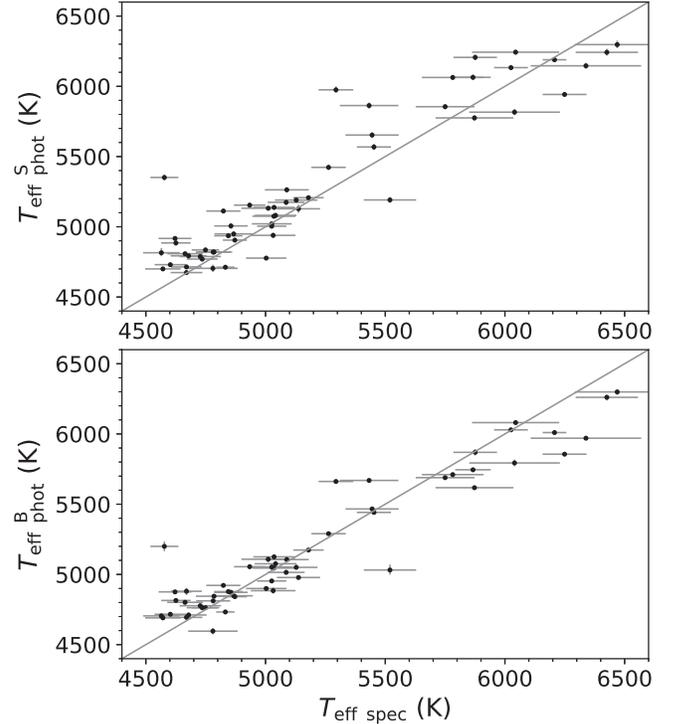

Figure 9. Top panels: the upper panel shows the single-star SED best-fit for one of the WD+AFGK binary candidates, TYC 3883-1104-1 (TGAS source ID: 1623107002022578304), while the lower panel shows the error-normalized residuals. Bottom panels: as above, but for the binary-star SED fit. The black dots represent the available photometry for this star. The red and blue spectra represent the best-fitting AFGK and WD models. The composite model spectrum of the WD+AFGK binary is shown in gray.

Figure 11 shows the comparison between the high-resolution spectroscopic $T_{\rm eff}$ and photometric $T_{\rm eff}$ (upper panel: single SED fitting $T_{\rm eff\ phot}^{S}$, bottom panel: binary SED fitting $T_{\rm eff\ phot}^{B}$). In the upper panel, the $T_{\rm eff}$ difference has a standard deviation of around 200 K. While in the bottom panel, when using the binary SED fitting $T_{\rm eff\ phot}^{B}$, the $T_{\rm eff}$ difference goes down to 178 K, which shows a relative improvement of $T_{\rm eff\,phot}$ when using binary SED fitting. The overall tendency is to find spectroscopic values slightly higher than the photometric ones ($\sim$50–150 K), a result that was also obtained for single stars by

Figure 11. Comparison of $T_{\rm eff}$ values obtained via the SED fitting, i.e., photometric (upper panel: $T_{\rm eff\ phot}^{S}$ from single SED fitting, bottom panel: $T_{\rm eff\ phot}^{B}$ from binary SED fitting) and those determined from the high-resolution spectra.

Zhou et al. (2019), especially above 5500 K. Although there is slight disagreement between $T_{\rm eff\,phot}$ and $T_{\rm eff\,spec}$ and our target selection is based on $T_{\rm eff\,phot}$, those targets with available high-resolution spectroscopic $T_{\rm eff}$ still fall well within our cuts as shown in Figure 1.
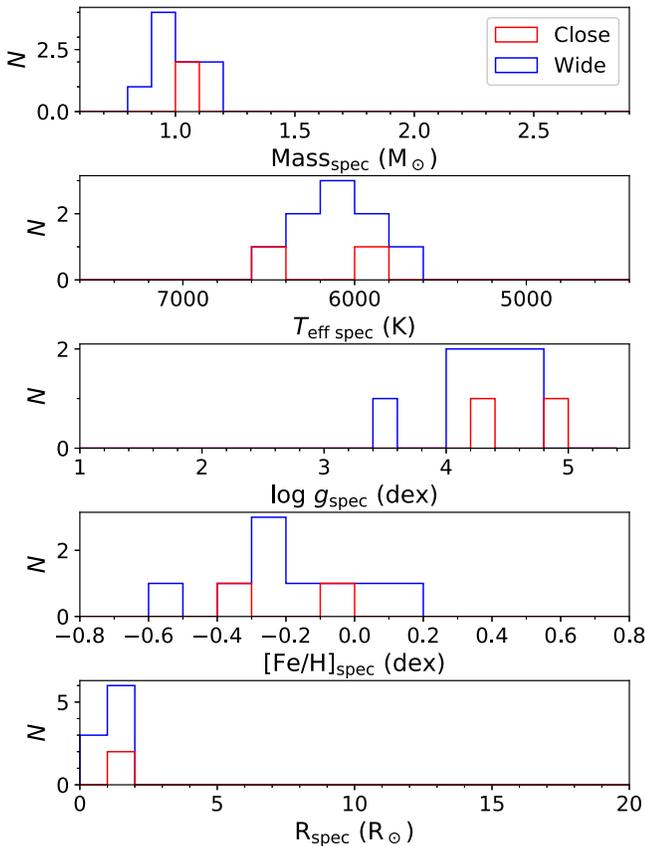
Figure 12. Histogram distributions of the high-resolution spectroscopic parameters of AFGK dwarfs (11) including mass, T_{eff}, $\log g$, [Fe/H], and radius. The red and blue lines show the close (2) and wide (9) WD+AFGK candidates respectively.

Figure 13. Similar to Figure 12, but for giants (44). The red and blue lines show the close (5) and wide (39) WD+AFGK candidates respectively.

6. Discussion

6.1. Close Binary Fraction

In our final sample, we have identified 23 close WD+AFGK binaries (13 dwarfs, 10 giants), and 128 wide binary candidates (64 dwarf, 64 giants) from our RV values. This translates into a close binary fraction of 15% (dwarf: 17%, giant: 14%).

As discussed in Paper II, the RVs measured from higher resolution spectra are more sensitive to detect binaries with longer ($\gtrsim 100$ days) orbital periods and lower ($\gtrsim 5$ deg) inclinations. Hence the close binary fraction measured from high-resolution spectroscopy should be more reliable.

If we only take into account the RVs measured from our XL216 and SPM high-resolution spectra, we find 19 close binary systems (10 dwarfs, 9 giants) and 85 wide binary candidates (32 dwarfs, 53 giants). Thus the close binary fraction is 18% (24% for dwarfs and 15% for giants).

The close binary fraction of WD+AFGK binaries harboring dwarf companions is higher than the 10% fraction we derived in Paper II. This can be explained as follows. First, the results from Paper II are based on a considerably smaller sample than the one used here (63 objects with high-resolution spectra). Second, and more importantly, the time baseline between the XL216 and SPM observations performed here is considerably larger than in the observations presented in Paper II, which allows us to identify longer-period systems.

Our results also indicate that $\sim$14% of our studied giant AFGK stars display RV variations. It is far away from the scope of this paper to confirm or disprove whether these variations are due to binary membership or pulsations (Wood et al. 2004;
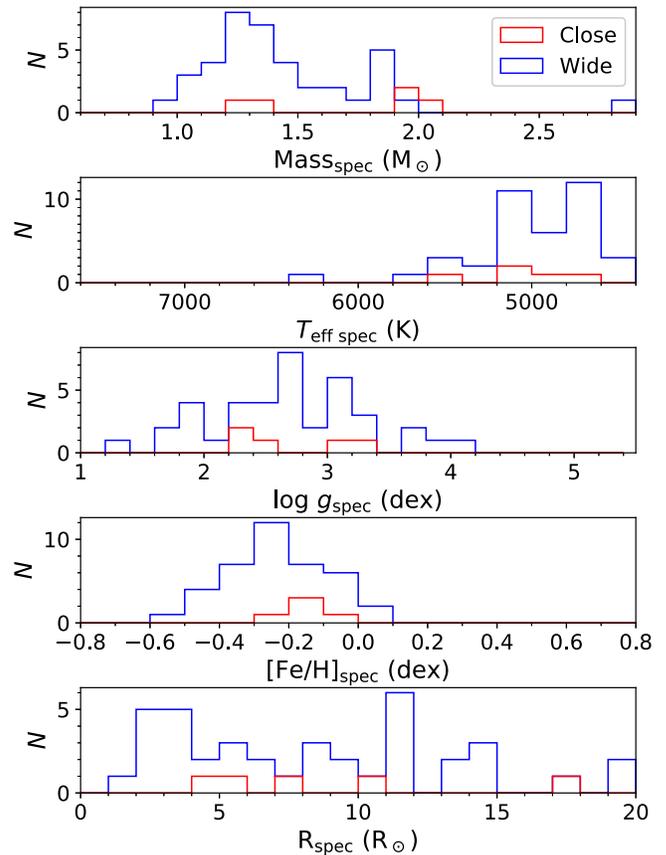
Nicholls et al. 2009) or other intrinsic mechanisms such as solar-type oscillations (Hekker 2007).

6.2. Stellar Parameter Distributions of the AFGK Stars

Based on the high-resolution spectroscopic parameters from Table A3, we present the distribution of stellar parameters (i.e., mass, T_{eff}, $\log g$, [Fe/H], and radius) of close/wide systems harboring AFGK dwarfs (11) in Figure 12. The parameter distribution of close/wide (2/9) systems are shown in red/blue color, respectively. From Figure 12, we can see that for these 11 AFGK dwarfs the masses cluster around $\sim$1.0 $M_\odot$. The mass distribution of close and wide binaries are very similar. The same is true for the T_{eff}, $\log g$, [Fe/H], and radius distributions. Both the close/wide systems have T_{eff} between 5600–6600 K, $\log g \sim$ 4–5 dex, [Fe/H] between -0.6 and $+0.1$ dex, radius between 0.85 and 1.3 $R_\odot$. A much larger sample of binaries harboring AFGK dwarfs with accurate high-resolution spectroscopic parameter determinations is necessary to further investigate possible differences between the stellar parameter distribution of close/wide binaries.

Figure 13 is similar to Figure 12, but represents the systems containing giant AFGK companions (44). It becomes obvious that the parameter distribution of these giants is very different from those arising from the dwarf sample. For the giants, both the close and wide systems have two mass peaks around 1.3 and 1.9 $M_\odot$. The distributions of T_{eff}, $\log g$, and radius of close and wide systems in giant samples do not show clear differences either. Unlike we found in the dwarf samples, the T_{eff} of the giant samples is clustered around a relatively colder temperature of
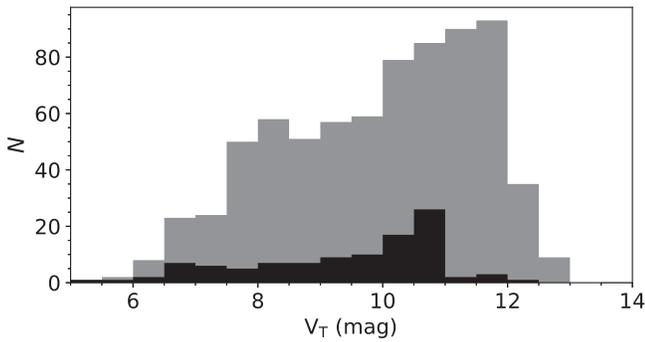
Figure 14. Histogram distribution of V_T magnitudes of all the WD+AFGK candidates (gray filled steps) and high-resolution spectroscopic observed ones by XL216 and SPM (black filled steps).

Figure 15. V_T magnitude vs. photometric T_{eff} for all the WD+AFGK candidates (gray dots), and those observed by XL216 (red dots), SPM (blue dots), and XL216+SPM (i.e., both observed by XL216 and SPM, green dots). The dots and triangles mark the dwarfs/giants respectively. The horizontal gray dashed line marks the $V_T = 11$ mag line. The upper small panel shows the histogram distribution of photometric T_{eff} of those high-resolution observed ones (black filled steps) and all the WD+AFGK candidates (gray filled steps).

Figure 16. Histogram distributions of T_{eff}^{WD} determined from binary SED fitting.

~ 5000 K. The [Fe/H] distribution of the giant samples are between -0.6 and 0.1 dex, which are very similar to the dwarf samples. It is also worth noting that the wide systems in the giant sample seem to be slightly metal-poor (peaks around -0.3 to -0.2 dex) as compared to those that are part of close systems (with a peak between -0.2 and -0.1 dex), which maybe due to the observational selection effect.

Furthermore, the stellar parameter distributions of close/wide systems we obtained here may suffer from observational selection effects. The telescopes we used are of two-meters (XL216 and SPM), which can only observe the very bright stars when equipped with a high-resolution Echelle spectrograph. In order to observe as many objects as possible and to improve the observation efficiency, we prioritized observations of the brighter objects in our sample. To put into contest this effect, in Figure 14 we show the histogram distributions of the V_T magnitudes of all the WD+AFGK candidates compared to those we observed at high-resolution. We can clearly see that the targets we observed are generally brighter than 11 mag, which is close to the limiting magnitude of the two-meter telescope equipped with high-resolution spectrograph.

To investigate possible observational selection effects on the parameter distributions, the bottom panel of Figure 15 shows the V_T versus photometric T_{eff} for all the WD+AFGK candidates and those with high-resolution observations. The upper panel shows their corresponding histogram distribution of T_{eff}. Inspection of the figure reveals the fraction of observed targets are relatively low near 6000 K (most are dwarfs), while most of the targets near 5000 K were observed due to their intrinsic brightness (most are giants). Thus, we can easily explain the difference between the T_{eff} distribution in Figures 12 and 13. But these observational selection effects do not affect the close binary fractions we measured in Section 6.1.

6.3. Stellar Parameter Distributions of WD

By using the binary SED fitting solutions for those WD +AFGK candidates with available high-resolution spectroscopic stellar parameters (in Table A3), the WD T_{eff} can be determined at the same time as described in Section 5.4. Figure 16 plots the histogram of the T_{eff}^{WD}. We can see that the distribution of WD T_{eff} has a peak around 10,000–30,000 K, which agrees with the T_{eff}^{WD} distributions from the WD+M binary sample (Rebassa-Mansergas et al. 2016).

6.4. Space Density of WD+AFGK Binaries

Our WD+AFGK binary sample has available Gaia parallaxes, hence it is possible to infer their distances. We obtain these values
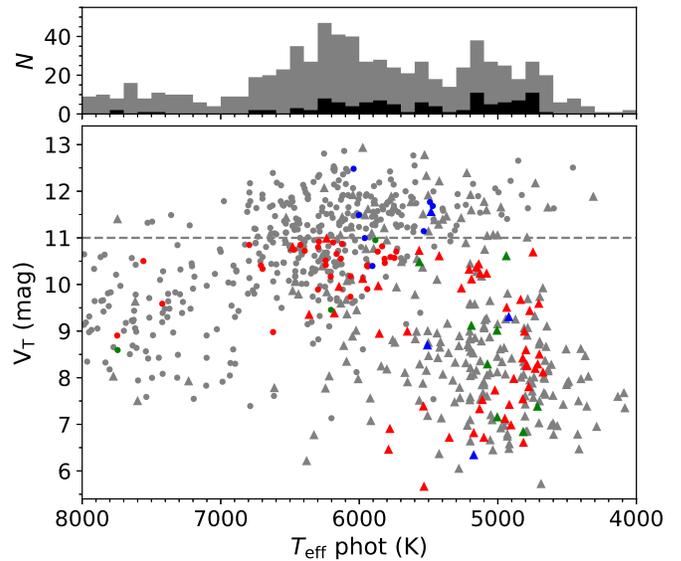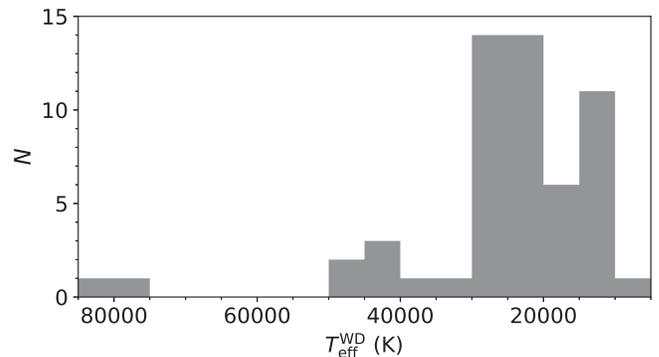
from the catalog of Bailer-Jones et al. (2018) and the corresponding histogram is shown in Figure 17, where we can see that our binaries are located in the $10 \sim 858$ pc range, peaking at ~ 250–300 pc. For comparison, Toonen et al. (2017) present a 20 pc sample of WD plus AFGKM main-sequence binaries (WDMS), which is more complete and includes 2 unresolved WDMS and 24 resolved WDMS. Our WD+AFGK sample extends this census up to ~ 850 pc, although it is not complete due to the possible incompleteness of Gaia or GALEX, especially in the Galactic plane, which is not covered by GALEX.

Jiménez-Esteban et al. (2018) analyze the completeness of the WD population accessible by Gaia as a function of the parallax relative error (see their Figure 1), from which it is possible to see how the distance affects the completeness of the Gaia WD sample. If we assume a similar distance effect in our binary sample, considering that the distance distribution of our WD +AFGK binaries peaks around 300 pc, we can assume a completeness of $\sim 50\%$ for our sample. If we further add the incompleteness of GALEX and the fact that we are biased toward
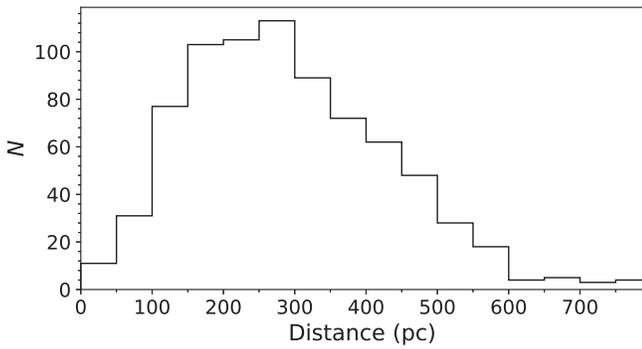
Figure 17. Histogram distributions of distances of the WD+AFGK binaries.

the detection of relatively hot WDs, then the completeness of our WD+AFGK sample should be severely lower than 50%.

From the distance information, we can estimate the space density ρ of our WD+AFGK binaries just integrating the number of objects in the volume considered and incorporating the scale height of the thin disk (322 pc, Chen et al. 2017) as a weighting factor in the integral (Schreiber & Gänsicke 2003). The calculation yields $\rho = 1.9 \times 10^{-6}$ pc^{-3}. However, as our sample is not complete, this value should be considered as a lower limit. Furthermore, with the aim of considering a volume-limited sample rather than a magnitude-limited one, we also estimate the space density for distances within 200 pc, which results in 10.5×10^{-6} pc^{-3}. Given that the WDs in these WD+AFGK binaries are generally hot, henceforth detectable via their UV excess, this result should also be considered as a lower limit.

7. Summary

As one of a series of papers aimed at constraining the past and future evolution of close compact binaries, here we presented the identification of WD+AFGK binaries from the TGAS and Gaia DR2 databases. We selected 814 WD+AFGK binary candidates through the detection of UV excess, out of which we selected 775 candidates after excluding possible contaminants. An extensive high-resolution spectroscopic follow-up campaign has been carried out to obtain at least two high-precision RVs separated at different nights for each of the selected WD+AFGK binaries. 214 high-resolution spectra ($R \sim 49{,}800$) were obtained from the Xinglong 2.16 m telescope for 93 WD+AFGK binary, and 50 high-resolution ($R \sim 20{,}000$) spectra were obtained for 22 WD+AFGK binaries. Furthermore, all the available spectroscopic sky survey data like LAMOST DR6 low-resolution spectra and RAVE DR5 medium-resolution spectra were also used to identify as many close binaries as possible.

We provide 517 RVs for 275 of our WD+AFGK binaries, from which we identify 23 close binaries via RV variations and 128 likely wide binaries. Interestingly, we find a relatively large percentage of WD+AFGK systems containing giants displaying RV variations. The close binary fraction we derive for WD+AFGK containing dwarf stars is around 24%. The close binary fraction for dwarf companions (24%) is higher than that for giant companions (15%). The atmospheric parameters ($T_{\rm eff}$, $\log g$, and [Fe/H]), as well as stellar mass and radius of the AFGK companions are provided from the high-resolution spectroscopy. The stellar parameters and mass distributions of the close and wide binaries are similar. Based on the Gaia distance, a lower limit of space density of WD+AFGK binary candidates is estimated to be 1.9×10^{-6} pc^{-3}, which increases to 10.5×10^{-6} pc^{-3} for samples within 200 pc.

Most of the close binaries found from this work are intrinsically bright (most are brighter than 11 mag), and thus will be easy to follow-up in the near future to measure their orbital periods and component masses. This will allow us to study the past and future evolution of these systems and thus improve our understanding of common envelope evolution and investigate possible formation channels for SN Ia.

Appendix

In this appendix we present the data table of the 814 selected WD+AFGK binary candidates (Table A1), the spectroscopic information of TGAS-RAVE/LAMOST WD+AFGK binaries (Table A2), and the high-resolution spectroscopic parameters of the AFGK companions in WD+AFGK binaries (Table A3).

Table A1
The 814 Selected WD+AFGK Binary Candidates

Name	Source ID (TGAS)	ϖ (TGAS) (mas)	B_T (mag)	V_T (mag)	FUV (mag)	NUV (mag)	Source ID (DR2)	α (DR2) (°)	δ (DR2) (°)	ϖ (DR2) (mas)	μ_α (mas yr^{-1})	μ_δ (mas yr^{-1})	G (mag)	G_{BP} (mag)	G_{RP} (mag)	$T_{\rm eff}$ (K)	R ($R_\odot$)	A_V (mag)	Dwarf	SIMBAD Classification	Contaminant	Spec	Flag
TYC 1006-4-1	4500804497016311040	2.847 ± 0.298	9.214 ± 0.017	7.986 ± 0.011	17.672 ± 0.057	15.751 ± 0.017	4500804501313209344	266.9840554690	14.7535113036	2.313 ± 0.052	0.092 ± 0.075	−18.014 ± 0.090	7.564	8.132	6.892	$4885.0^{+20.0}_{-20.0}$	$18.86^{+0.33}_{-0.40}$	$0.25^{+0.02}_{-0.02}$	N	Star	N	⋯	⋯
TYC 1007-942-1	4476095172207240704	3.592 ± 0.465	9.687 ± 0.024	9.436 ± 0.022	13.192 ± 0.007	13.485 ± 0.003	4476095176502659584	269.8479409744	7.7092128037	3.724 ± 0.043	−6.981 ± 0.068	−7.211 ± 0.065	9.391	9.512	9.204	$7625.0^{+37.0}_{-35.0}$	$1.81^{+0.02}_{-0.02}$	$0.08^{+0.01}_{-0.01}$	Y	Star	N	⋯	⋯
TYC 1010-2134-1	4478719603379517568	2.449 ± 0.265	10.324 ± 0.027	10.098 ± 0.029	14.372 ± 0.013	13.674 ± 0.004	4478719607687083904	275.6919592219	8.8715466865	2.261 ± 0.052	−3.762 ± 0.074	5.089 ± 0.083	9.956	10.102	9.734	$7438.0^{+32.0}_{-32.0}$	$2.41^{+0.05}_{-0.05}$	$0.10^{+0.01}_{-0.01}$	Y	Star	N	⋯	⋯
TYC 1010-403-1	4481708041623948672	2.127 ± 0.285	11.400 ± 0.063	11.412 ± 0.098	14.684 ± 0.011	14.173 ± 0.004	4481708045927762944	274.5910736665	9.1088137354	1.727 ± 0.044	4.205 ± 0.078	2.734 ± 0.073	11.056	–	–	$7745.0^{+63.0}_{-66.0}$	$1.94^{+0.04}_{-0.04}$	$0.30^{+0.02}_{-0.02}$	N	Star	N	LAMOST	⋯
TYC 1012-788-1	4494712721561721728	2.733 ± 0.266	9.469 ± 0.020	8.540 ± 0.014	14.404 ± 0.015	13.492 ± 0.006	4494712725861730176	270.0509389652	10.5163424463	2.060 ± 0.067	2.853 ± 0.119	2.763 ± 0.119	8.184	8.682	7.556	$5356.0^{+24.0}_{-25.0}$	$13.55^{+0.31}_{-0.37}$	$0.47^{+0.01}_{-0.02}$	N	Star	N	⋯	⋯
TYC 1020-875-1	4498214219417652608	1.930 ± 0.247	12.596 ± 0.193	12.183 ± 0.170	18.254 ± 0.083	15.789 ± 0.018	4498214219417652608	271.7589501457	14.6368243940	1.836 ± 0.041	5.025 ± 0.074	3.240 ± 0.073	11.923	12.172	11.533	$6595.0^{+32.0}_{-31.0}$	$1.56^{+0.03}_{-0.02}$	$0.14^{+0.01}_{-0.01}$	Y	Star	N	LAMOST	⋯
TYC 1023-2378-1	4477623459012735488	4.301 ± 0.306	13.069 ± 0.262	11.763 ± 0.134	17.051 ± 0.047	16.623 ± 0.027	4477623459012735488	277.2176435238	7.8490471591	4.253 ± 0.048	6.571 ± 0.088	−1.306 ± 0.088	11.645	12.024	11.120	$5895.0^{+28.0}_{-28.0}$	$1.00^{+0.00}_{-0.00}$	$0.26^{+0.02}_{-0.02}$	Y	Star	N	⋯	⋯
TYC 1027-1804-1	4480505210263029632	3.045 ± 0.276	12.458 ± 0.187	11.551 ± 0.110	18.275 ± 0.087	16.689 ± 0.030	4480505214573963520	276.9209151405	10.5316866686	3.917 ± 0.052	−4.483 ± 0.085	0.261 ± 0.087	11.290	11.659	10.765	$5718.0^{+19.0}_{-19.0}$	$1.29^{+0.01}_{-0.01}$	$0.07^{+0.01}_{-0.01}$	Y	Star	N	⋯	⋯
TYC 1031-707-1	4485165902619270656	3.399 ± 0.334	9.415 ± 0.020	9.198 ± 0.018	12.932 ± 0.008	12.859 ± 0.005	4485165906920932864	276.4871821339	12.7786034894	3.691 ± 0.041	−8.628 ± 0.070	−5.475 ± 0.072	9.142	9.248	8.986	$7861.0^{+36.0}_{-37.0}$	$1.89^{+0.02}_{-0.02}$	$0.00^{+0.00}_{-0.00}$	Y	Variable Star	N	⋯	⋯
TYC 103-810-1	3234843885583146880	2.494 ± 0.305	10.170 ± 0.033	9.972 ± 0.033	13.259 ± 0.006	13.284 ± 0.006	3234843889879946880	77.2968945732	2.1784489294	2.281 ± 0.043	−2.006 ± 0.081	−12.144 ± 0.054	9.881	10.019	9.650	$7101.0^{+28.0}_{-30.0}$	$2.95^{+0.03}_{-0.02}$	$0.18^{+0.00}_{-0.01}$	Y	Star	N	⋯	⋯
TYC 110-755-1	3240025986963617792	7.477 ± 0.229	11.202 ± 0.074	10.570 ± 0.063	16.882 ± 0.039	14.936 ± 0.009	3240025986963617792	76.7235053441	6.1154965611	7.326 ± 0.065	−13.519 ± 0.093	−9.512 ± 0.076	10.300	10.663	9.808	$5746.0^{+22.0}_{-23.0}$	$1.12^{+0.01}_{-0.01}$	$0.15^{+0.01}_{-0.01}$	Y	Star	N	⋯	⋯
TYC 1117-2238-1	1758854975332493568	3.363 ± 0.280	9.554 ± 0.024	8.896 ± 0.018	17.615 ± 0.057	13.374 ± 0.005	1758854979627147776	318.5411607094	13.2453330926	3.099 ± 0.039	−2.073 ± 0.072	−7.297 ± 0.061	8.635	8.970	8.170	$6049.0^{+23.0}_{-23.0}$	$5.12^{+0.07}_{-0.07}$	$0.21^{+0.01}_{-0.01}$	N	Star	N	⋯	⋯
TYC 1134-190-1	1768992369459334272	3.283 ± 0.248	9.789 ± 0.022	9.209 ± 0.017	18.146 ± 0.046	14.134 ± 0.004	1768992369459334272	328.6807253391	14.5576497717	3.329 ± 0.048	−8.680 ± 0.072	−22.244 ± 0.069	8.697	9.064	8.196	$5517.0^{+18.0}_{-18.0}$	$5.13^{+0.08}_{-0.08}$	$0.00^{+0.00}_{-0.00}$	N	Eclipsing binary of Algol type	Y	⋯	⋯
TYC 1134-414-1	1768986562663551104	2.776 ± 0.278	9.512 ± 0.019	9.243 ± 0.017	14.931 ± 0.010	13.853 ± 0.004	1768986566959444096	328.6396538629	14.5347921319	2.873 ± 0.058	14.001 ± 0.084	−1.838 ± 0.089	9.178	9.308	8.980	$7538.0^{+30.0}_{-30.0}$	$2.63^{+0.05}_{-0.05}$	$0.08^{+0.01}_{-0.01}$	Y	Eclipsing binary	Y	⋯	⋯
⋯	⋯	⋯	⋯	⋯	⋯	⋯	⋯	⋯	⋯	⋯	⋯	⋯	⋯	⋯	⋯	⋯	⋯	⋯	⋯	⋯	⋯	⋯	⋯

Note. Here we list the name, TGAS source ID, parallax, Tycho $B_T V_T$ magnitudes, GALEX photometry, Gaia DR2 coordinate on epoch of 2015.5, parallax, proper motion, $G/G_{BP}/G_{RP}$ magnitudes, the SED fitting results, the dwarf/giant classification ("Dwarf = Y" shows dwarf, "N" is giant), the SIMBAD classification, the contaminant flag ("Contaminant = Y" shows the possible contaminant, "N" shows our final sample), and whether it has available spectra from RAVE DR5 or LAMOST DR6 (column "Spec"). The last column marks if it has already been published before, where "flag = a" means published in the RAVE WD+AFGK sample from Paper I, "flag = b" shows those published in the LAMOST WD+AFGK sample from Paper II, and "flag = −" shows the new ones that were unpublished before. The entire table is provided in the electronic version of the paper.

(This table is available in its entirety in machine-readable form.)

Table A2
The Spectroscopic Information of TGAS-RAVE/LAMOST WD+AFGK Binaries

Name	HJD (days)	S/N	$T_{\rm eff}$ (K)	log g (dex)	Metallicity (dex)	Flag
TYC 1010-403-1	2457860.34272	220.67	⋯	⋯	⋯	LAMOST
TYC 1010-403-1	2457917.19322	223.53	⋯	⋯	⋯	LAMOST
TYC 1020-875-1	2457528.30082	87.18	6808.76 ± 23.13	4.053 ± 0.038	−0.139 ± 0.022	LAMOST
TYC 12-20-1	2456199.24772	1.56	⋯	⋯	⋯	LAMOST
TYC 1246-582-1	2457018.06924	261.65	⋯	⋯	⋯	LAMOST
TYC 1246-582-1	2457662.37084	5.43	⋯	⋯	⋯	LAMOST
TYC 1246-850-1	2457662.37087	493.05	⋯	⋯	⋯	LAMOST
TYC 1287-1768-1	2456946.36737	439.64	⋯	⋯	⋯	LAMOST
TYC 1380-957-1	2456283.23496	156.63	5915.45 ± 19.50	4.321 ± 0.032	0.130 ± 0.017	LAMOST
TYC 1389-1680-1	2458168.07737	205.37	5719.85 ± 21.30	3.987 ± 0.034	0.008 ± 0.018	LAMOST
TYC 1428-81-1	2457444.25195	6.34	⋯	⋯	⋯	LAMOST
TYC 1451-111-1	2456021.14327	142.35	⋯	⋯	⋯	LAMOST
TYC 1451-111-1	2457435.39474	267.49	6217.27 ± 11.67	4.255 ± 0.017	−0.198 ± 0.009	LAMOST
TYC 1451-111-1	2457438.31629	3.65	⋯	⋯	⋯	LAMOST
TYC 1478-39-1	2456757.25111	121.55	⋯	⋯	⋯	LAMOST
TYC 1507-49-1	2457475.34315	0.33	⋯	⋯	⋯	LAMOST
TYC 1557-1803-1	2457497.31875	421.86	6371.38 ± 13.33	4.100 ± 0.018	−0.221 ± 0.011	LAMOST
TYC 1719-425-1	2456202.13169	9.65	⋯	⋯	⋯	LAMOST
TYC 1742-1301-1	2456551.17560	458.08	5814.84 ± 11.86	4.278 ± 0.016	−0.169 ± 0.010	LAMOST
TYC 1742-1301-1	2456551.21249	394.91	5828.02 ± 12.11	4.300 ± 0.017	−0.159 ± 0.010	LAMOST
TYC 1742-1301-1	2457327.11410	516.72	5831.32 ± 14.65	4.356 ± 0.020	−0.160 ± 0.012	LAMOST
TYC 1749-1463-1	2456589.20749	166.29	6381.57 ± 15.88	4.207 ± 0.026	−0.038 ± 0.014	LAMOST
TYC 1758-2133-1	2456202.25293	9.68	⋯	⋯	⋯	LAMOST
TYC 1761-51-1	2456202.22094	540.92	⋯	⋯	⋯	LAMOST
TYC 1768-162-1	2456675.98709	268.90	⋯	⋯	⋯	LAMOST
TYC 1783-665-1	2456571.27033	272.20	5532.58 ± 17.39	4.383 ± 0.026	−0.748 ± 0.014	LAMOST
TYC 1783-665-1	2457356.16870	315.84	5565.33 ± 17.42	4.400 ± 0.024	−0.736 ± 0.014	LAMOST
TYC 1784-1075-1	2456571.27034	426.26	6491.27 ± 10.73	4.152 ± 0.015	0.022 ± 0.009	LAMOST
TYC 1784-1075-1	2457356.16872	513.54	6518.88 ± 8.56	4.149 ± 0.012	−0.001 ± 0.007	LAMOST
TYC 1821-1013-1	2456663.00263	359.90	6618.26 ± 20.61	4.141 ± 0.029	−0.319 ± 0.017	LAMOST
TYC 1821-1013-1	2456967.27996	183.26	6611.93 ± 15.11	4.120 ± 0.024	−0.276 ± 0.013	LAMOST
TYC 1914-31-1	2456280.28387	146.54	6980.44 ± 37.64	4.072 ± 0.062	0.291 ± 0.034	LAMOST
TYC 1986-2176-1	2457003.42890	173.38	5859.00 ± 18.25	4.407 ± 0.030	−0.175 ± 0.016	LAMOST
TYC 1986-2176-1	2457528.03422	177.26	5825.61 ± 21.79	4.340 ± 0.035	−0.229 ± 0.019	LAMOST
TYC 2023-752-1	2458138.42031	259.92	5620.74 ± 15.63	4.154 ± 0.024	−0.511 ± 0.013	LAMOST
TYC 2027-86-1	2456063.15284	99.70	6358.69 ± 23.44	4.284 ± 0.039	−0.279 ± 0.022	LAMOST
TYC 2027-86-1	2456084.07977	77.06	6304.67 ± 25.67	4.249 ± 0.042	−0.321 ± 0.024	LAMOST
TYC 2036-1214-1	2457085.35397	188.02	6177.14 ± 12.47	4.294 ± 0.020	−1.120 ± 0.011	LAMOST
TYC 2036-1214-1	2458256.23926	43.16	6150.94 ± 69.68	4.188 ± 0.115	−1.193 ± 0.067	LAMOST
TYC 2298-197-1	2457297.27205	520.90	6699.88 ± 9.60	4.209 ± 0.013	−0.195 ± 0.008	LAMOST
TYC 2336-231-1	2456255.18835	456.74	6922.95 ± 9.72	4.210 ± 0.013	−0.518 ± 0.008	LAMOST
TYC 236-1252-1	2455974.17818	161.87	5591.08 ± 30.89	4.275 ± 0.050	−0.164 ± 0.027	LAMOST
TYC 236-1252-1	2457026.29595	94.45	5587.54 ± 25.24	4.243 ± 0.042	−0.197 ± 0.024	LAMOST
TYC 2472-1279-1	2457358.35211	149.82	6121.30 ± 21.22	4.339 ± 0.035	0.152 ± 0.019	LAMOST
TYC 2506-1107-1	2456769.05532	98.86	5872.37 ± 29.96	4.212 ± 0.049	−0.203 ± 0.028	LAMOST
⋯	⋯	⋯	⋯	⋯	⋯	⋯

Note. Here we list the name, Heliocentric Julian Dates (HJD) of the RAVE/LAMOST spectrum, S/N, and stellar parameters (the $T_{\rm eff}$, log g, and metallicity of the companion; for RAVE data, metallicity is the [m/H], while for LAMOST, it is the [Fe/H]). The last column flags the origin of the data, i.e., RAVE or LAMOST. "⋯" indicates that no parameter is available. The entire table is provided in the electronic version of the paper.

(This table is available in its entirety in machine-readable form.)

Table A3
The High-resolution Spectroscopic Parameters of the AFGK Companions in WD+AFGK Binaries

Name	$T_{\rm eff}$ (K)	$\log g$ (dex)	[Fe/H] (dex)	M ($M_\odot$)	R ($R_\odot$)	$T_{\rm eff}^{B}$ (K)	R^{B} ($R_\odot$)	A_V^{B} (mag)	$T_{\rm eff}^{\rm WD}$ (K)
TYC 1006-4-1	4625.50 ± 61.37	1.76 ± 0.25	−0.29 ± 0.05	1.816 ± 0.227	19.369 ± 0.935	$4814.62^{+14.15}_{-14.27}$	$19.0436^{+0.4298}_{-0.4094}$	$0.1603^{+0.0236}_{-0.0237}$	$13772.61^{+703.98}_{-593.66}$
TYC 1223-498-1	5519.67 ± 109.43	3.27 ± 0.22	−0.06 ± 0.07	1.919 ± 0.057	5.125 ± 0.271	$5031.45^{+38.37}_{-33.86}$	$6.9760^{+0.1158}_{-0.1120}$	$0.0842^{+0.0326}_{-0.0322}$	$12545.90^{+132.42}_{-116.82}$
TYC 1385-562-1	6249.07 ± 91.65	4.67 ± 0.12	0.02 ± 0.03	1.082 ± 0.012	0.965 ± 0.018	$5855.99^{+3.25}_{-3.29}$	$0.9805^{+0.0013}_{-0.0012}$	$0.0011^{+0.0018}_{-0.0008}$	$24959.86^{+1219.91}_{-1384.18}$
TYC 1394-1008-1	5866.53 ± 74.29	4.33 ± 0.10	−0.05 ± 0.04	1.006 ± 0.038	1.072 ± 0.035	$5744.94^{+6.83}_{-6.34}$	$1.1744^{+0.0077}_{-0.0077}$	$0.0042^{+0.0065}_{-0.0031}$	$24147.18^{+1770.95}_{-1751.50}$
TYC 1451-111-1	6468.99 ± 177.41	4.27 ± 0.31	−0.09 ± 0.11	1.136 ± 0.049	1.142 ± 0.041	$6299.14^{+15.69}_{-19.30}$	$1.1974^{+0.0085}_{-0.0084}$	$0.0338^{+0.0123}_{-0.0167}$	$15548.81^{+975.14}_{-891.00}$
TYC 1506-1141-1	4621.81 ± 68.75	1.82 ± 0.23	−0.30 ± 0.05	1.414 ± 0.205	14.287 ± 0.699	$4875.68^{+5.11}_{-1.192}$	$12.9464^{+0.1234}_{-0.1192}$	$0.0077^{+0.0108}_{-0.0057}$	$45643.73^{+4487.39}_{-4213.62}$
TYC 169-1942-1	5128.14 ± 88.94	3.18 ± 0.20	−0.29 ± 0.07	1.496 ± 0.164	5.815 ± 0.336	$5050.26^{+19.38}_{-15.75}$	$5.9781^{+0.1739}_{-0.1683}$	$0.0182^{+0.0212}_{-0.0128}$	$29638.87^{+2496.00}_{-2315.95}$
TYC 1707-426-1	5445.06 ± 111.04	3.88 ± 0.15	−0.06 ± 0.07	1.387 ± 0.034	2.703 ± 0.156	$5465.98^{+10.09}_{-7.06}$	$2.7895^{+0.0207}_{-0.0211}$	$0.0148^{+0.0165}_{-0.0104}$	$26724.66^{+2142.78}_{-1987.48}$
TYC 1742-1301-1	5781.96 ± 128.93	4.22 ± 0.16	−0.24 ± 0.08	0.929 ± 0.045	1.015 ± 0.036	$5710.58^{+14.57}_{-10.63}$	$1.1277^{+0.0053}_{-0.0052}$	$0.0156^{+0.0169}_{-0.0110}$	$21191.01^{+1770.96}_{-1718.14}$
TYC 1911-715-1	5088.65 ± 91.69	3.12 ± 0.13	−0.37 ± 0.07	1.209 ± 0.126	4.674 ± 0.202	$5105.53^{+6.87}_{-6.15}$	$4.5763^{+0.0736}_{-0.0713}$	$0.0067^{+0.0101}_{-0.0049}$	$26123.30^{+2120.45}_{-2003.80}$
TYC 2471-204-1	6040.18 ± 189.32	4.12 ± 0.28	0.14 ± 0.11	1.162 ± 0.059	1.288 ± 0.076	$5793.54^{+24.01}_{-22.89}$	$1.4242^{+0.0127}_{-0.0127}$	$0.0330^{+0.0236}_{-0.0213}$	$13383.08^{+703.20}_{-504.33}$
TYC 2488-308-1	5263.17 ± 71.98	3.62 ± 0.13	−0.09 ± 0.06	1.262 ± 0.035	2.485 ± 0.106	$5290.02^{+10.86}_{-9.49}$	$2.5593^{+0.0337}_{-0.0337}$	$0.0084^{+0.0125}_{-0.0061}$	$22355.87^{+1716.63}_{-1668.80}$
TYC 26-39-1	4669.59 ± 66.42	2.21 ± 0.24	−0.11 ± 0.05	1.399 ± 0.199	11.787 ± 0.640	$4694.15^{+9.24}_{-8.54}$	$12.3935^{+0.2032}_{-0.2037}$	$0.0256^{+0.0198}_{-0.0164}$	$14971.66^{+1037.23}_{-931.88}$
TYC 2719-866-1	5002.65 ± 84.29	2.62 ± 0.11	−0.20 ± 0.07	1.786 ± 0.313	9.789 ± 0.541	$4899.69^{+10.41}_{-10.22}$	$12.9727^{+0.1823}_{-0.1771}$	$0.1779^{+0.0221}_{-0.0239}$	$14576.59^{+891.67}_{-759.24}$
TYC 278-239-1	5025.76 ± 61.00	2.55 ± 0.05	−0.16 ± 0.05	1.903 ± 0.040	7.914 ± 0.113	$4953.34^{+3.63}_{-3.13}$	$8.5409^{+0.1011}_{-0.1020}$	$0.0043^{+0.0069}_{-0.0032}$	$27815.45^{+2293.53}_{-2045.45}$
TYC 3029-161-1	5750.19 ± 122.95	3.65 ± 0.21	−0.30 ± 0.08	1.224 ± 0.039	2.352 ± 0.120	$5688.84^{+4.37}_{-3.62}$	$2.4765^{+0.0139}_{-0.0139}$	$0.0029^{+0.0048}_{-0.0022}$	$15611.92^{+1147.50}_{-1023.82}$
TYC 3067-471-1	5035.63 ± 86.97	3.31 ± 0.19	−0.19 ± 0.06	1.100 ± 0.085	2.798 ± 0.119	$5124.99^{+7.63}_{-7.02}$	$2.7150^{+0.0199}_{-0.0204}$	$0.0116^{+0.0112}_{-0.0082}$	$21808.58^{+1676.78}_{-1523.54}$
TYC 3080-957-1	5011.12 ± 112.08	2.60 ± 0.11	−0.16 ± 0.09	1.826 ± 0.386	9.139 ± 0.536	$5108.10^{+17.45}_{-21.68}$	$8.9227^{+0.0639}_{-0.0604}$	$0.0434^{+0.0154}_{-0.0221}$	$10084.66^{+139.80}_{-119.18}$
TYC 3094-108-1	5025.96 ± 83.34	2.29 ± 0.10	−0.25 ± 0.06	1.896 ± 0.259	8.842 ± 0.339	$5052.48^{+20.85}_{-22.95}$	$9.2675^{+0.0922}_{-0.0949}$	$0.0402^{+0.0170}_{-0.0212}$	$12042.18^{+86.57}_{-81.67}$
TYC 3097-697-1	4844.55 ± 59.32	2.81 ± 0.10	−0.48 ± 0.05	0.935 ± 0.028	3.709 ± 0.085	$4877.60^{+6.94}_{-6.72}$	$4.0443^{+0.0234}_{-0.0226}$	$0.0054^{+0.0082}_{-0.0041}$	$28991.00^{+2086.19}_{-1932.04}$
TYC 3251-1514-1	4832.12 ± 38.32	2.55 ± 0.13	−0.13 ± 0.05	1.650 ± 0.189	11.230 ± 0.374	$4732.67^{+14.32}_{-15.15}$	$12.7203^{+0.2665}_{-0.2605}$	$0.0313^{+0.0239}_{-0.0195}$	$13241.68^{+618.90}_{-483.93}$
TYC 3453-106-1	5294.10 ± 72.33	3.13 ± 0.08	−0.21 ± 0.07	1.419 ± 0.051	3.341 ± 0.159	$5661.83^{+8.41}_{-7.78}$	$2.8238^{+0.0305}_{-0.0309}$	$0.0036^{+0.0059}_{-0.0027}$	$30346.15^{+2607.33}_{-2344.61}$
TYC 3457-852-1	5179.28 ± 63.73	3.32 ± 0.14	−0.20 ± 0.04	1.277 ± 0.050	2.904 ± 0.113	$5173.64^{+7.50}_{-6.92}$	$2.9022^{+0.0227}_{-0.0231}$	$0.0072^{+0.0103}_{-0.0051}$	$23960.14^{+1756.03}_{-1767.68}$
TYC 3464-912-1	6025.19 ± 70.62	4.74 ± 0.04	−0.26 ± 0.06	0.969 ± 0.038	1.110 ± 0.032	$6029.25^{+7.09}_{-6.79}$	$0.9970^{+0.0002}_{-0.0002}$	$0.0017^{+0.0029}_{-0.0013}$	$20827.18^{+1519.67}_{-1443.20}$
TYC 3640-1105-1	6338.37 ± 230.87	4.19 ± 0.21	−0.09 ± 0.13	1.284 ± 0.074	1.692 ± 0.125	$5969.77^{+6.92}_{-5.74}$	$1.9378^{+0.0129}_{-0.0126}$	$0.0047^{+0.0071}_{-0.0035}$	$42266.62^{+3803.86}_{-3888.82}$
TYC 368-1591-1	4564.74 ± 75.95	1.29 ± 0.28	−0.45 ± 0.07	1.294 ± 0.242	19.543 ± 0.891	$4704.78^{+7.68}_{-7.72}$	$20.6288^{+0.2484}_{-0.2459}$	$0.1908^{+0.0235}_{-0.0253}$	$24547.35^{+1963.13}_{-1881.66}$
TYC 3807-183-1	5452.71 ± 71.24	3.04 ± 0.08	−0.59 ± 0.08	1.863 ± 0.057	6.274 ± 0.287	$5441.60^{+4.76}_{-3.63}$	$6.1730^{+0.1377}_{-0.1344}$	$0.0043^{+0.0065}_{-0.0032}$	$76159.38^{+6939.21}_{-6904.40}$
TYC 3808-1388-1	4784.63 ± 76.06	2.72 ± 0.20	−0.08 ± 0.06	1.394 ± 0.146	8.110 ± 0.415	$4844.79^{+8.44}_{-8.90}$	$7.8196^{+0.1341}_{-0.1324}$	$0.0608^{+0.0223}_{-0.0226}$	$24980.53^{+1925.63}_{-1825.22}$
TYC 3816-790-1	4602.23 ± 65.74	1.76 ± 0.25	−0.25 ± 0.04	1.192 ± 0.151	11.412 ± 0.758	$4716.33^{+6.51}_{-6.51}$	$11.4287^{+0.1468}_{-0.1447}$	$0.0072^{+0.0098}_{-0.0054}$	$22035.62^{+1638.69}_{-1615.52}$
TYC 3829-462-1	5872.74 ± 162.5	4.52 ± 0.16	−0.33 ± 0.10	0.884 ± 0.041	0.855 ± 0.027	$5617.50^{+7.38}_{-6.24}$	$1.0336^{+0.0018}_{-0.0018}$	$0.0114^{+0.0098}_{-0.0079}$	$21892.30^{+1747.86}_{-1713.74}$
TYC 3841-492-1	4871.77 ± 50.17	2.75 ± 0.21	−0.35 ± 0.04	1.333 ± 0.14	10.827 ± 0.255	$4841.72^{+3.48}_{-3.23}$	$11.4237^{+0.0704}_{-0.0694}$	$0.0045^{+0.0066}_{-0.0033}$	$21404.70^{+1706.91}_{-1653.05}$
TYC 3868-840-1	4571.12 ± 74.05	1.81 ± 0.33	−0.38 ± 0.08	1.084 ± 0.115	11.424 ± 0.585	$4690.68^{+5.64}_{-5.07}$	$11.3052^{+0.1159}_{-0.1171}$	$0.0094^{+0.0121}_{-0.0069}$	$23682.25^{+1915.22}_{-1797.60}$
TYC 3881-159-1	6044.66 ± 182.18	4.14 ± 0.28	−0.11 ± 0.14	1.011 ± 0.061	1.038 ± 0.045	$6080.76^{+8.73}_{-8.34}$	$0.9597^{+0.0022}_{-0.0022}$	$0.0030^{+0.0049}_{-0.0022}$	$26083.32^{+1629.60}_{-1533.22}$
TYC 3883-1104-1	5041.81 ± 87.45	3.04 ± 0.15	−0.18 ± 0.07	1.289 ± 0.125	4.647 ± 0.208	$5075.79^{+20.46}_{-20.61}$	$4.3722^{+0.0647}_{-0.0659}$	$0.0186^{+0.0197}_{-0.0133}$	$26823.48^{+2115.15}_{-1922.99}$
TYC 405-806-1	4779.99 ± 103.41	2.22 ± 0.32	−0.23 ± 0.10	1.097 ± 0.116	5.365 ± 0.249	$4596.19^{+22.20}_{-22.96}$	$6.9271^{+0.0998}_{-0.0996}$	$0.1980^{+0.0288}_{-0.0298}$	$17081.07^{+1209.56}_{-1179.26}$
TYC 4102-715-1	5137.58 ± 90.20	3.31 ± 0.20	−0.42 ± 0.07	1.082 ± 0.101	3.120 ± 0.132	$4978.02^{+12.63}_{-12.94}$	$3.6467^{+0.0414}_{-0.0420}$	$0.1519^{+0.0257}_{-0.0261}$	$27642.26^{+2397.45}_{-2219.99}$
TYC 4219-2017-1	4933.69 ± 65.93	2.63 ± 0.13	−0.28 ± 0.04	1.114 ± 0.103	4.503 ± 0.160	$5054.83^{+17.75}_{-13.58}$	$4.2871^{+0.0377}_{-0.0379}$	$0.0164^{+0.0197}_{-0.0118}$	$27689.55^{+2104.84}_{-1995.40}$
TYC 4220-740-1	4663.71 ± 74.65	2.62 ± 0.21	−0.03 ± 0.09	1.108 ± 0.096	5.585 ± 0.220	$4801.32^{+13.99}_{-14.73}$	$5.4827^{+0.0455}_{-0.0455}$	$0.0661^{+0.0233}_{-0.0221}$	$19012.61^{+1399.74}_{-1354.81}$
TYC 4352-264-1	4577.29 ± 58.63	1.85 ± 0.25	−0.32 ± 0.05	1.562 ± 0.177	17.183 ± 0.703	$5199.71^{+34.46}_{-34.61}$	$13.4281^{+0.1395}_{-0.1347}$	$0.1919^{+0.0323}_{-0.0319}$	$9843.75^{+46.53}_{-46.24}$
TYC 4385-1146-1	6207.12 ± 49.36	4.44 ± 0.09	−0.52 ± 0.08	0.945 ± 0.039	0.954 ± 0.018	$6009.88^{+5.95}_{-4.27}$	$0.9565^{+0.0023}_{-0.0023}$	$0.0035^{+0.0057}_{-0.0026}$	$28351.92^{+1816.02}_{-1642.59}$
TYC 4442-1466-1	4823.69 ± 71.36	1.98 ± 0.12	−0.49 ± 0.06	1.511 ± 0.233	13.627 ± 0.649	$4921.83^{+7.18}_{-5.67}$	$13.4331^{+0.1143}_{-0.1111}$	$0.0235^{+0.0195}_{-0.0153}$	$35113.69^{+3494.33}_{-3109.63}$
TYC 4559-684-1	4727.17 ± 86.43	2.20 ± 0.25	−0.20 ± 0.09	1.416 ± 0.219	11.601 ± 0.677	$4777.10^{+5.23}_{-4.51}$	$12.0509^{+0.1170}_{-0.1175}$	$0.0091^{+0.0124}_{-0.0066}$	$28701.19^{+2466.28}_{-2284.57}$

Table A3
(Continued)

Name	$T_{\rm eff}$ (K)	$\log g$ (dex)	[Fe/H] (dex)	M ($M_\odot$)	R ($R_\odot$)	$T_{\rm eff}{}^B$ (K)	R^B ($R_\odot$)	A_V^B (mag)	$T_{\rm eff}{}^{\rm WD}$ (K)
TYC 4564-627-1	6425.64 ± 130.34	4.93 ± 0.05	-0.30 ± 0.10	1.097 ± 0.054	1.175 ± 0.045	$6260.69^{+17.54}_{-22.35}$	$1.2987^{+0.0065}_{-0.0066}$	$0.1174^{+0.0169}_{-0.0220}$	$82073.84^{+5350.56}_{-7220.90}$
TYC 4574-366-1	4866.91 ± 79.95	2.59 ± 0.14	-0.12 ± 0.06	1.302 ± 0.130	6.240 ± 0.259	$4847.98^{+8.01}_{-6.43}$	$6.4107^{+0.0340}_{-0.0312}$	$0.0219^{+0.0196}_{-0.0145}$	$19247.88^{+1556.12}_{-1480.54}$
TYC 4615-1151-1	4678.50 ± 75.22	2.15 ± 0.23	-0.31 ± 0.06	1.259 ± 0.173	11.346 ± 0.688	$4711.35^{+8.10}_{-7.93}$	$13.5254^{+0.1545}_{-0.1522}$	$0.1445^{+0.0216}_{-0.0210}$	$26950.68^{+2192.92}_{-2095.20}$
TYC 4649-3689-1	5086.06 ± 77.21	2.81 ± 0.26	0.08 ± 0.07	2.814 ± 0.093	14.284 ± 0.478	$5014.5^{+17.96}_{-11.25}$	$14.0749^{+0.1692}_{-0.1647}$	$0.0195^{+0.0212}_{-0.0130}$	$21503.37^{+1718.39}_{-1586.80}$
TYC 4665-621-1	4735.21 ± 64.45	2.64 ± 0.08	-0.02 ± 0.05	1.361 ± 0.121	7.646 ± 0.330	$4762.97^{+7.74}_{-7.63}$	$7.5859^{+0.1250}_{-0.1232}$	$0.0119^{+0.0153}_{-0.0088}$	$18703.70^{+1315.26}_{-1228.61}$
TYC 4681-1527-1	5432.54 ± 122.25	3.14 ± 0.18	-0.24 ± 0.09	1.364 ± 0.055	3.007 ± 0.246	$5669.19^{+7.40}_{-4.58}$	$2.8611^{+0.0850}_{-0.0839}$	$0.0066^{+0.0101}_{-0.0049}$	$28520.66^{+2389.20}_{-2313.95}$
TYC 4685-1113-1	4748.91 ± 57.54	2.49 ± 0.14	-0.19 ± 0.06	1.897 ± 0.267	14.203 ± 0.945	$4762.70^{+10.03}_{-8.85}$	$14.4456^{+0.6254}_{-0.5439}$	$0.0164^{+0.0189}_{-0.0116}$	$40773.74^{+3702.39}_{-3563.79}$
TYC 4698-895-1	5031.75 ± 93.31	3.13 ± 0.15	0.10 ± 0.07	1.285 ± 0.094	3.127 ± 0.170	$4884.34^{+22.37}_{-20.98}$	$3.3165^{+0.0489}_{-0.0477}$	$0.0254^{+0.0244}_{-0.0180}$	$14663.98^{+772.14}_{-624.36}$
TYC 4717-255-1	4669.64 ± 64.60	2.27 ± 0.21	-0.14 ± 0.05	2.038 ± 0.206	17.590 ± 0.783	$4880.21^{+23.15}_{-27.20}$	$17.1540^{+0.3213}_{-0.3098}$	$0.2326^{+0.0289}_{-0.0320}$	$11066.93^{+169.69}_{-149.24}$
TYC 4831-473-1	5875.75 ± 91.00	3.52 ± 0.14	-0.23 ± 0.08	0.940 ± 0.044	1.048 ± 0.035	$5869.21^{+23.50}_{-21.86}$	$1.1074^{+0.0054}_{-0.0055}$	$0.0551^{+0.0281}_{-0.0263}$	$29737.52^{+2523.61}_{-2483.18}$
TYC 5-436-1	4781.09 ± 71.07	2.47 ± 0.09	-0.28 ± 0.06	1.697 ± 0.263	13.607 ± 0.732	$4811.54^{+6.67}_{-8.04}$	$14.2855^{+0.3045}_{-0.3002}$	$0.0608^{+0.0120}_{-0.0178}$	$49015.12^{+4668.07}_{-4754.36}$
TYC 856-918-1	4855.40 ± 70.04	2.37 ± 0.09	-0.21 ± 0.05	1.304 ± 0.243	10.522 ± 0.422	$4872.50^{+10.91}_{-11.48}$	$11.1999^{+0.2670}_{-0.2749}$	$0.0732^{+0.0240}_{-0.0247}$	$44185.79^{+4312.38}_{-4261.46}$
TYC 877-681-1	5034.89 ± 89.67	2.63 ± 0.18	-0.19 ± 0.07	1.928 ± 0.071	8.088 ± 0.230	$5045.09^{+20.76}_{-18.02}$	$8.1619^{+0.1444}_{-0.1412}$	$0.0187^{+0.0218}_{-0.0133}$	$11744.89^{+152.26}_{-143.00}$

Note. Here we list the stellar parameters ($T_{\rm eff}$, $\log g$, and [Fe/H]), mass and radius determined from high-resolution spectra, the $T_{\rm eff}{}^B$, R^B, and A_V^B of AFGK companions, and $T_{\rm eff}^{\rm WD}$ of WD estimated from binary SED fitting solution.

ORCID iDs

J.-J. Ren ● https://orcid.org/0000-0003-3243-464X
R. Raddi ● https://orcid.org/0000-0002-9090-9191
A. Rebassa-Mansergas ● https://orcid.org/0000-0002-6153-7173
S. G. Parsons ● https://orcid.org/0000-0002-2695-2654
P. Irawati ● https://orcid.org/0000-0002-3348-1491
M. R. Schreiber ● https://orcid.org/0000-0003-3903-8009
B. T. Gänsicke ● https://orcid.org/0000-0002-2761-3005
Y. Zhao ● https://orcid.org/0000-0002-4391-2822
Y.-T. Zhou ● https://orcid.org/0000-0002-4410-9740
B. Wang ● https://orcid.org/0000-0002-3231-1167
C. Liu ● https://orcid.org/0000-0002-1802-6917
J.-R. Shi ● https://orcid.org/0000-0002-0349-7839
H. Tian ● https://orcid.org/0000-0003-3347-7596

References

Astropy Collaboration, Price-Whelan, A. M., Sipőcz, B. M., et al. 2018, AJ, 156, 123
Astropy Collaboration, Robitaille, T. P., Tollerud, E. J., et al. 2013, A&A, 558, A33
Bailer-Jones, C. A. L., Rybizki, J., Fouesneau, M., Mantelet, G., & Andrae, R. 2018, AJ, 156, 58
Bianchi, L., Shiao, B., & Thilker, D. 2017, ApJS, 230, 24
Blanco-Cuaresma, S. 2019, MNRAS, 486, 2075
Blanco-Cuaresma, S., Soubiran, C., Heiter, U., & Jofré, P. 2014, A&A, 569, A111
Breedt, E., Steeghs, D., Marsh, T. R., et al. 2017, MNRAS, 468, 2910
Bressan, A., Marigo, P., Girardi, L., et al. 2012, MNRAS, 427, 127
Chen, B. Q., Liu, X. W., Yuan, H. B., et al. 2017, MNRAS, 464, 2545
Choi, J., Dotter, A., Conroy, C., et al. 2016, ApJ, 823, 102
Cui, X.-Q., Zhao, Y.-H., Chu, Y.-Q., et al. 2012, RAA, 12, 1197
da Silva, L., Girardi, L., Pasquini, L., et al. 2006, A&A, 458, 609
de Kool, M. 1992, A&A, 261, 188
Duchêne, G., & Kraus, A. 2013, ARA&A, 51, 269
Fan, Z., Wang, H., Jiang, X., et al. 2016, PASP, 128, 115005
Fitzpatrick, E. L. 1999, PASP, 111, 63
Flörs, A., Spyromilio, J., Taubenberger, S., et al. 2020, MNRAS, 491, 2902
Foreman-Mackey, D., Farr, W., Sinha, M., et al. 2019, JOSS, 4, 1864
Gaia Collaboration, Brown, A. G. A., Vallenari, A., et al. 2016a, A&A, 595, A2
Gaia Collaboration, Brown, A. G. A., Vallenari, A., et al. 2018, A&A, 616, A1
Gaia Collaboration, Prusti, T., de Bruijne, J. H. J., et al. 2016b, A&A, 595, A1
Gänsicke, B. T., Dillon, M., Southworth, J., et al. 2009, MNRAS, 397, 2170
Geier, S. 2020, A&A, 635, A193
Gray, R. O., & Corbally, C. J. 1994, AJ, 107, 742
Grevesse, N., Asplund, M., & Sauval, A. J. 2007, SSRv, 130, 105
Gustafsson, B., Edvardsson, B., Eriksson, K., et al. 2008, A&A, 486, 951
Han, Z., & Podsiadlowski, P. 2004, MNRAS, 350, 1301
Heiter, U., Lind, K., Asplund, M., et al. 2015, PhyS, 90, 054010
Hekker, S. 2007, PhD thesis, Leiden Univ.
Henden, A. A., Levine, S., Terrell, D., & Welch, D. L. 2015, AAS Meeting, 225, 336.16
Hernandez, M. S., Schreiber, M. R., Parsons, S. G., et al. 2020, MNRAS, submitted
Høg, E., Fabricius, C., Makarov, V. V., et al. 2000, A&A, 355, L27
Husser, T. O., Wende-von Berg, S., Dreizler, S., et al. 2013, A&A, 553, A6
Iben, I. J., & Livio, M. 1993, PASP, 105, 1373
Jiménez-Esteban, F. M., Torres, S., Rebassa-Mansergas, A., et al. 2018, MNRAS, 480, 4505
Kalomeni, B., Nelson, L., Rappaport, S., et al. 2016, ApJ, 833, 83
Kilic, M., Brown, W. R., Gianninas, A., et al. 2017, MNRAS, 471, 4218
Koester, D. 2010, MmSAI, 81, 921
Kordopatis, G., Gilmore, G., Steinmetz, M., et al. 2013, AJ, 146, 134
Kunder, A., Kordopatis, G., Steinmetz, M., et al. 2017, AJ, 153, 75

Lagos, F., Schreiber, M. R., Parsons, S. G., et al. 2020, MNRAS, 494, 915
Langer, N., Deutschmann, A., Wellstein, S., & Höflich, P. 2000, A&A, 362, 1046
Lindegren, L., Hernández, J., Bombrun, A., et al. 2018, A&A, 616, A2
Lindegren, L., Lammers, U., Bastian, U., et al. 2016, A&A, 595, A4
Liu, C., Fu, J., Shi, J., et al. 2020, arXiv:2005.07210
Luo, A. L., Zhao, Y.-H., Zhao, G., et al. 2015, RAA, 15, 1095
Maíz Apellániz, J. 2006, AJ, 131, 1184
Maíz Apellániz, J., & Pantaleoni González, M. 2018, A&A, 616, L7
Maíz Apellániz, J., & Weiler, M. 2018, A&A, 619, A180
Maoz, D., & Mannucci, F. 2012, PASA, 29, 447
Maoz, D., Mannucci, F., & Brandt, T. D. 2012, MNRAS, 426, 3282
Michalik, D., Lindegren, L., & Hobbs, D. 2015, A&A, 574, A115
Munari, U., Henden, A., Frigo, A., et al. 2014, AJ, 148, 81
Nelemans, G., Yungelson, L. R., Portegies Zwart, S. F., & Verbunt, F. 2001, A&A, 365, 491
Newville, M., Stensitzki, T., Allen, D. B., & Ingargiola, A. 2014, LMFIT: Non-Linear Least-Square Minimization and Curve-Fitting for Python, 0.8.0, Zenodo, doi:10.5281/zenodo.11813
Nicholls, C. P., Wood, P. R., Cioni, M. R. L., & Soszyński, I. 2009, MNRAS, 399, 2063
Paczynski, B. 1976, in IAU Symp. 73, Structure and Evolution of Close Binary Systems, ed. P. Eggleton, S. Mitton, & J. Whelan (Dordrecht: Reidel), 75
Pala, A. F., Gänsicke, B. T., Townsley, D., et al. 2017, MNRAS, 466, 2855
Parsons, S. G., Rebassa-Mansergas, A., Schreiber, M. R., et al. 2016, MNRAS, 463, 2125
Parsons, S. G., Schreiber, M. R., Gänsicke, B. T., et al. 2015, MNRAS, 452, 1754
Parthasarathy, M., Branch, D., Jeffery, D. J., & Baron, E. 2007, NewAR, 51, 524
Passy, J.-C., De Marco, O., Fryer, C. L., et al. 2012, ApJ, 744, 52
Perlmutter, S., Aldering, G., Goldhaber, G., et al. 1999, ApJ, 517, 565
Prugniel, P., & Soubiran, C. 2001, A&A, 369, 1048
Rebassa-Mansergas, A., Gänsicke, B. T., Rodríguez-Gil, P., Schreiber, M. R., & Koester, D. 2007, MNRAS, 382, 1377
Rebassa-Mansergas, A., Parsons, S. G., García-Berro, E., et al. 2017a, MNRAS, 466, 1575
Rebassa-Mansergas, A., Ren, J. J., Irawati, P., et al. 2017b, MNRAS, 472, 4193
Rebassa-Mansergas, A., Ren, J. J., Parsons, S. G., et al. 2016, MNRAS, 458, 3808
Ren, J., Luo, A., Li, Y., et al. 2013, AJ, 146, 82
Ren, J. J., Rebassa-Mansergas, A., Parsons, S. G., et al. 2018, MNRAS, 477, 4641
Ricker, P. M., & Taam, R. E. 2012, ApJ, 746, 74
Riess, A. G., Filippenko, A. V., Challis, P., et al. 1998, AJ, 116, 1009
Schlegel, D. J., Finkbeiner, D. P., & Davis, M. 1998, ApJ, 500, 525
Schreiber, M. R., & Gänsicke, B. T. 2003, A&A, 406, 305
Skrutskie, M. F., Cutri, R. M., Stiening, R., et al. 2006, AJ, 131, 1163
Soker, N. 2018, SCPMA, 61, 49502
Tody, D. 1986, Proc. SPIE, 627 (0627), 733
Tody, D. 1993, in ASP Conf. Ser. 52, IRAF in the Nineties, ed. R. J. Hanisch, R. J. V. Brissenden, & J. Barnes (San Francisco, CA: ASP), 173
Toonen, S., Hollands, M., Gänsicke, B. T., & Boekholt, T. 2017, A&A, 602, A16
Virtanen, P., Gommers, R., Oliphant, T. E., et al. 2020, Nature Methods, 17, 261
Wang, B. 2018, RAA, 18, 049
Wang, B., & Han, Z. 2012, NewAR, 56, 122
Wang, B., Li, X.-D., & Han, Z.-W. 2010, MNRAS, 401, 2729
Webbink, R. F. 2008, in Common Envelope Evolution Redux, Astrophysics and Space Science Library, ed. E. F. Milone, D. A. Leahy, & D. W. Hobill (Berlin: Springer), 233
Wenger, M., Ochsenbein, F., Egret, D., et al. 2000, A&AS, 143, 9
Whelan, J., & Iben, I. J. 1973, ApJ, 186, 1007
Willems, B., & Kolb, U. 2004, A&A, 419, 1057
Wood, P. R., Olivier, E. A., & Kawaler, S. D. 2004, ApJ, 604, 800
Wright, E. L., Eisenhardt, P. R. M., Mainzer, A. K., et al. 2010, AJ, 140, 1868
Zhou, Y., Yan, H., Shi, J., et al. 2019, ApJ, 877, 104